MULTIFILTER SPECTROPHOTOMETRY OF THE ENVIRONMENT OF THE QUASAR 3C281

By

Sally Eve Craven

B. Sc. (Astronomy) University of Victoria

A THESIS SUBMITTED IN PARTIAL FULFILLMENT OF

THE REQUIREMENTS FOR THE DEGREE OF

MASTER OF SCIENCE

in

THE FACULTY OF GRADUATE STUDIES

GEOPHYSICS AND ASTRONOMY

We accept this thesis as conforming

to the required standard

THE UNIVERSITY OF BRITISH COLUMBIA

April 1993

In presenting this thesis in partial fulfilment of the requirements for an advanced degree at the University of British Columbia, I agree that the Library shall make it freely available for reference and study. I further agree that permission for extensive copying of this thesis for scholarly purposes may be granted by the head of my department or by his or her representatives. It is understood that copying or publication of this thesis for financial gain shall not be allowed without my written permission.

Geophysics and Astronomy
The University of British Columbia
2075 Wesbrook Place
Vancouver, Canada
V6T 1Z1

Date: April 30th, 1997

Abstract

The technique of multifilter spectrophotometry is applied to identify stars and deduce galaxy redshifts and morphological types in a field centred on the quasar 3C281, with the intention of both testing the method and identifying members of the galaxy cluster surrounding the QSO. Photometry is performed on CCD images taken in twenty-four narrowband filters, and the resulting spectral energy distributions are compared with redshifted model galaxy spectra from Rocca-Volmerange and Guiderdoni (1988) and with fiducial star spectra from Gunn and Stryker (1983) to determine the physical characteristics of the best-fitting spectral template. For twelve of the 184 objects in the 3.7'×6' field, spectroscopic redshifts have been published (Ellingson, Green, and Yee 1991), and an attempt is made to examine the accuracy of the technique using this small sample: a relationship between object signal-to-noise ratio and error in assigned redshift is sought.

The results of a complementary study using simulated spectral energy distributions (Callaghan, Gibson, and Hickson 1992; Callaghan 1992) are briefly described, and compared with results from this data set.

A broadband R filter is simulated by combining twenty-one narrowband filters, and the instrumental magnitudes are calibrated with published magnitudes from Yee, Green, and Stockman (1986). The photometric errors are found to increase substantially with decreasing signal-to-noise ratio, but the results suggest that broadband multicolour photometry could be fairly accurately performed for many of the objects in the field, if the

appropriate narrowband filters were present. Of the commonly used broadband filters UBVRI, this data set has spectral coverage adequate to simulate only the R filter.

Multifilter spectrophotometry has the potential to be a versatile and efficient survey technique, and will be employed in the sky survey to be made in forty filters by the UBC Liquid Mirror Telescope (Hickson et al. 1993, Gibson & Hickson 1991).

Contents

List of Tables

List of Figures

Acknowledgements

I would first like to express my gratitude to my supervisor, Dr. Paul Hickson, who gave me the opportunity to work on a fascinating project with many possibilities, and in so doing taught me that nothing in astronomy is ever as straightforward as it looks at first. I would also like to acknowledge his financial support over the last two and a half years, and offer my thanks to him for making it possible for me to attend graduate school. Thanks are also due to the co-data-owner and collaborator Dr. Howard Yee, professional optimist ("You know, the data look cleaner than I thought they would") and author of PPP, who was always prepared to suggest a new way to approach the problem. I thank Dr. Claudia Mendes de Oliveira for helpful discussions and much-needed encouragement at the right time, and Dr. Greg Fahlman and Dr. Harvey Richer for perceptive and valuable comments on this thesis.

I must offer my thanks to my fellow graduate students, many of whom have helped me through the rough spots. Brad Gibson was always ready to help on questions about galaxy spectra and evolution, filters, the LMT, computers, and just about anything else. Ted Kennelly exhibited boundless and contagious enthusiasm for astronomy, career development, artistic impression, and life in general. He was also really good about the Victoria Inner Harbour UFO incident. (Vergessen Sie nicht: dem Blinden hilft keine Brille.) Phil Hodder provided invaluable assistance with extended LaTeX tutorial sessions, and knew the short answer to every computer question I ever asked. Dave Hogg ("astonomer"), Dave Woods, and Andy Walker, among many other things, helped straighten out my understanding of the theory and practice of error analysis, for which I am indebted to all three. Every astronomy student in this department has been supportive throughout the last few years; my thanks to all of them.

I'm forever grateful to my family, who have always encouraged me and have never once remarked on the job prospects in astronomy. Thanks, you guys.

Thanks to Pat Durrell (*aka* Tarpick Di Rella, Hatrack Umbrella, and Josie of the Quasi-Stellar Sheep Ranchers), for friendly competition ("By the way, I'm finishing my thesis this weekend"), years of conversation about astronomy and other things, preprints, many movies, and reams of email.

Last but by no means least, my thanks to my husband Scott Tinis – for keeping me happy, keeping me sane, and keeping me from sleeping in. May it last forever.

Chapter 1

Introduction

The study of the large-scale structure and evolution of the universe requires extensive samples of galaxy redshifts to test cosmological models. In particular, redshifts of faint galaxies are needed to extend the physical limits of the surveys deeper into the universe. The best way to obtain the necessary numbers of faint-galaxy redshifts is to use a big telescope dedicated to a survey project, but it is difficult for a single project to claim enough observing time for an extensive faint-object redshift survey.

With large liquid mirror telescopes (Hickson, Gibson, and Hogg 1993; Gibson and Hickson 1991) it is possible to have an inexpensive, and therefore private, telescope which can be dedicated to a redshift survey. In fact, since the reflecting surface of a liquid mirror telescope is composed of mercury forming a parabolic shape due to rotation of the mirror, such telescopes are zenith-pointing instruments and are therefore intended as survey "machines". Because the telescope can only point at the zenith, it cannot track on individual objects and conventional spectroscopy is difficult (although not impossible; it is conceivable that one could employ a grism, or moving slits or fibres — P. Hickson, pers. comm.). However, low-resolution spectral energy distributions (SEDs) of objects in the field of view can be obtained by observing through numerous narrowband filters using a large-format CCD operated in driftscanning mode, read out at the speed with which

the image moves across the chip.

The goal of this thesis is to explore the method of multifilter spectrophotometry, or analysis of the spectral energy distributions produced by performing photometry on the images in the multiple narrowband filters. In parallel with a separate analysis of simulated data (Callaghan, Gibson, and Hickson 1992; Callaghan 1992; Hickson, Gibson, and Callaghan 1993; and also reviewed in chapter 6 of this thesis), some problems with the method are identified and the accuracy of the results investigated.

1.1 History

In the days of photographic spectra, the Palomar Observatory responded to the need for spectroscopy of faint objects by developing a nine-filter photometric system, reaching from the ultraviolet (3730 Å) to the infrared K (9875 Å). Baum (1962) used this equipment to produce early magnitude-redshift plots in an attempt to fit observations to world models.

Shortly thereafter, a prime-focus photoelectric spectrum scanner (Oke 1966) was built at Palomar. This instrument was designed to obtain spectral energy distributions (SEDs) of sources to about 19th magnitude in "a reasonable amount of observing time". That observing time was determined by both the brightness of the source and the chosen spectral resolution, usually between 50Å and 200Å. The instrument was tunable to any wavelength and bandwidth in its allowed range, but was only able to measure light in one band at a time. Such single-channel photoelectric scanners were popular in the late 1960s: the Lick Observatory also had a pulse-counting prime-focus scanning spectrophotometer, which sampled the spectrum every 100Å with bandwidth 60Å in the red and 45Å in the blue (Wampler, 1966, 1967).

Spectrum scanners were efficient instruments (Oke 1969) because of their wide band-

passes, small number of reflecting surfaces, and high quantum efficiency photomultipliers. However, observations of objects fainter than 19th magnitude were not practical due to background sky limitations. Spectrographs at that time had useful limiting magnitudes of about 20, since their slits admitted less sky than the scanner apertures. The goal of the observers was to push back the magnitude limits at which usable spectroscopic information could be obtained, and that inspired the construction of a multichannel photoelectric spectrometer at Palomar.

The multichannel spectrometer, first mounted on the 200-inch telescope in 1968, was described by Oke (1969). Its thirty-three simultaneous channels covered a spectral range from the atmospheric limit, near 3100Å to 11000Å, where water vapour significantly contaminates the spectrum. Even before the blue channels of the spectrometer were functional, useful results could be obtained: Oke, Neugebauer, and Becklin (1970) presented a set of QSO observations made in part with the spectrometer over a range of 5600Å to 11000Å, in fifteen channels with bandwidths of 360Å. The multichannel spectrophotometer data are similar in nature to the data from the multi-narrowband filter system described in this thesis.

1.2 Perspective

The development of linear integrated array detectors, with their increased detection efficiency, immensely improved faint-end limits for spectrographs. However, the best limits of state-of-the-art instruments are never considered good enough, as witnessed by the unceasing demand for larger numbers of redshifts in a smaller amount of observing time. Today, the observer can choose from at least three approaches besides conventional spectroscopy: multi-object spectrography, multicolour photometry, and multifilter spectrophotometry.

Most large telescopes have among their instrumentation a multi-object spectrograph of some type. Whether employing optical fibres or masks with multiple slits, these instruments allow one to make use of more of the light collected by the telescope than in ordinary single-slit spectroscopy, by simultaneously obtaining spectra of a number of objects in the field. Multi-object spectrographs are particularly suited to galaxy cluster studies (see for example Ellingson, Green, and Yee 1991). Their main advantage over the other two techniques described below is the resolution of the spectra obtained, typically on the order of 15 Å. MOSs, however, are not ideal survey instruments: the observer must know which are the target objects, such as cluster members, and must have accurate positions for all of them. The number of target objects is also limited, by the field size, chip size, and desired spectral resolution; but this is a minor limitation in view of the ability of a MOS to obtain many spectra at reasonably high resolution in a short time.

Multicolour photometry has also been used to find redshifts of faint galaxies. Baum (1962) showed that photometry of a galaxy in nine colours, using the Palomar pulse-counting photoelectric photometer, permitted its redshift to be determined by identifying the position of the 4000Å break. In 1980, H. Spinrad, in a discussion of methods of locating high-redshift elliptical galaxies to use as standard candles, suggested "a new method" of using the colour signature of high-redshift E/S0 galaxies to identify them in the vicinity of quasars, and showed that it was possible to detect evolution in these galaxies. Broadband photometry of galaxies in clusters has often been used to describe the morphological makeup of the cluster population (where the cluster redshift is known); for example, see papers referred to by Couch et al.(1983): Butcher & Oemler (1978a), Couch & Newall (1980), Mathieu & Spinrad (1981), Koo (1981).

D. Koo (1981, 1985) made use of Baum's ideas and an extensive literature of previous work on two-colour plots of galaxies at low and high redshifts, to prove that colour-colour

plots, calibrated with Bruzual's (1983) model galaxy spectra, can be an effective tool for estimating galaxy redshifts. His agreement with spectroscopic redshifts for a sample of one hundred galaxies of magnitude 17 to 23 is quite impressive: for redshifts below 0.35, two-thirds of the eighty redshifts agree with spectroscopic values within ± 0.04. Complications of an approach of this type to redshift determination include the effects of galaxy evolution, dust, and reddening (internal and external to the galaxy in question). The advantages over multi-slit or multiple narrow-band filter approaches are the shorter observing times required in the broadband filters and the ability to compensate for poor detector sensitivity in the blue by taking longer exposures.

The third of these options is a compromise between multi-object spectroscopy and multicolour photometry, including the flexibility and blue sensitivity of colour-colour analyses while providing higher resolution and making the effects of spectral evolution more evident. Multifilter spectrophotometry provides data similar to that from the the multichannel spectrum scanner. It employs photometry of CCD images made in a single field through a number of narrow-band filters, and has the potential to produce hundreds of spectral energy distributions in a field, depending on the nature and size of the field and on the length of the exposures. It is suited to an exploratory approach: the observer need not select the particular objects for which spectra are to be obtained as with multi-object spectroscopy, but may rather investigate the character of a field in any location, whether it be set on a galaxy cluster or elsewhere. The spectral range and resolution depend on the choice of number, central wavelength, and bandwidth of the filters, and the depth of the data set is controlled by the filter characteristics as well as the amount of observing time available. The quality of the spectral energy distributions, however, is highly dependent on the accuracy of the photometry in all the filters.

To improve spectral resolution, narrower filter bandpasses are needed, and therefore

the exposure times must be longer. For a limited field, a multi-object spectrograph can provide a lot of high-resolution spectra in the same time required for a multifilter study. However, surveys over large areas can benefit from the exploratory nature of the multifilter approach, especially in the case of a zenith-pointing telescope like the UBC Liquid Mirror Telescope discussed later in this section.

The key to the technique of multifilter spectrophotometry is to find a spectral template which best fits the spectral energy distribution of a given object, as opposed to seeking a colour difference which crosses the 4000 Å break. In principle, this allows one to determine the redshift and morphological classification of the source. Couch et al. (1983), Ellis et al. (1983), and MacLaren et al. (1988) used six intermediate-band filters and three Hubble-type templates at a range of redshifts to study the populations of galaxy clusters. Part of their goal was to investigate the effects of galaxy evolution upon the method. Loh & Spillar (1986), with their six intermediate-band filters and three fiducial galaxy templates (which were linearly interpolated to construct templates of intermediate type) estimated redshifts for approximately a thousand galaxies. The position and size of the 4000Å break were the primary criteria in making the fit, but the rest of the shape of the spectral energy distribution was also considered. Successful comparisons of some of their results with published spectroscopic redshifts led them to conclude that the technique was successful in determining accurate redshifts for both early and late-type galaxies.

Despite the promise of multi-filter "redshift machines", cluster studies can only be carried out to a certain level with these low-resolution spectral energy distributions. Ultimately, higher resolution is needed for fine dynamical structure studies. A complementary approach incorporating both multifilter spectrophotometry and multi-object spectroscopy could provide very useful results, in particular if the former is used to find targets of interest for the latter.

The real power of multifilter spectrophotometry is its application to surveys. In particular, it is an essential part of the survey to be carried out by the University of British Columbia Liquid Mirror Telescope (or LMT) (Hickson et al. 1993; Gibson & Hickson 1991). The present UBC LMT has a 2.7-metre-diameter reflecting surface, and forty narrow- and intermediate-band filters will be used in a driftscan-survey of a strip of sky twenty arcminutes wide and of total area thirteen square degrees. The survey is expected to take two years, and to observe 10000 galaxies and 1000 QSOs during that time. The relatively low cost of building such telescopes makes them ideal survey instruments, and the intention of the UBC group is to follow this experiment with a larger LMT.

The primary reason for undertaking the project described in this thesis was to test the narrowband filter technique of obtaining redshifts and morphological classifications to be used for the LMT project, although cluster fields of scientific interest, containing a quasar apparently at the centre of a cluster of galaxies, were chosen as targets. Previous work in the area of multifilter spectrophotometry has been expanded upon: the SEDs are constructed from twenty-four filters of much narrower bandwidth than previous groups have used, and the fiducial spectra include seven galaxy types and eighty-one stellar spectra. The galaxy templates are redshifted from zero to one in increments of about 0.01 for comparison with the spectral energy distributions.

The redshifts obtained from this technique are expected to be accurate enough to identify members of the cluster surrounding the quasar, and to describe the population and distribution of galaxies in the cluster down to a certain magnitude limit. Surveys of fields such as this can also provide information on the morphology of the field galaxy population.

Chapter 2

The Data and the Reductions

2.1 The Filter Set

A multifilter approach to studying galaxy clusters, as compared to higher-resolution multi-slit observations, has the advantage of efficiency: all objects in the cluster are observed simultaneously, with no need for an observer to identify the few cluster members or objects of interest beforehand to create the mask; and less light is lost in a filter system than in a spectrograph. It is also less expensive than a multi-object spectrograph, as the cost depends on the quality of the filters. This is a prime consideration for a dedicated survey telescope which may be operated by a small institution or by an individual.

The filter set used for these data was substantially less expensive and therefore of lower quality (in terms of peak transmission value and transmission curve shape) than the set of filters now in place on the UBC Liquid Mirror Telescope. Figure 2.1 shows the transmission curves [1] for the twenty-four filters used to observe the field surrounding the QSO 3C281. The filter bandpasses are approximately 100Å wide at their half-maximum point, with equivalent widths on the order of 50 to 70Å. The equivalent widths of the filters are listed in table 2.1, and table 2.2 contains the data for the filter transmission curves.

[1] These data were obtained from the Corion Corporation, manufacturers of the filters.

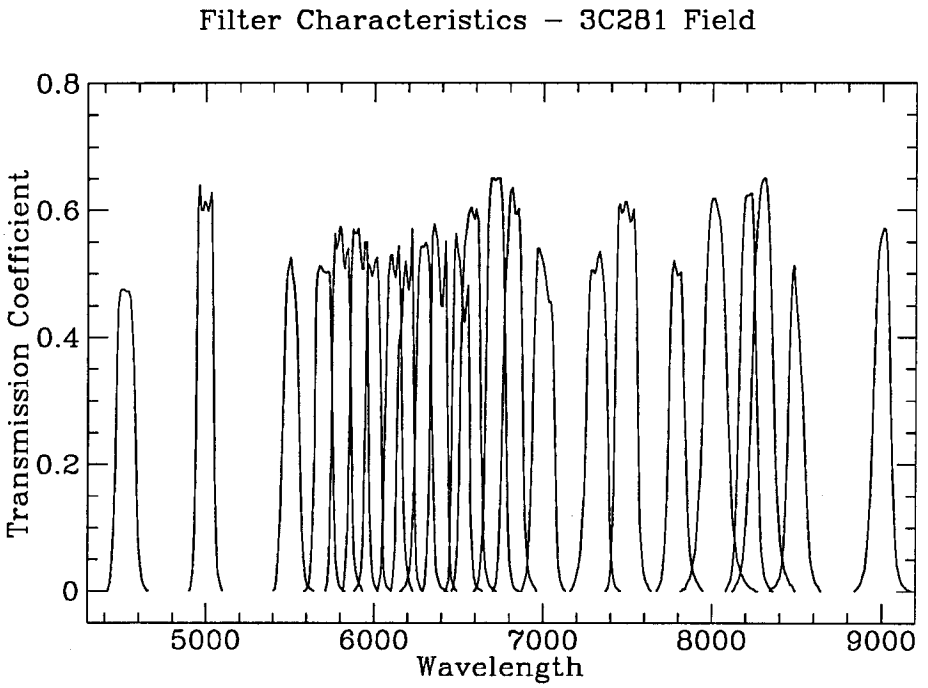

Figure 2.1: The transmission curves used for the twenty-four filters in the 3C281 field. (Data from Corion Corp.)

Table 2.1: The equivalent widths of the filters

Filter λ	Equivalent width (Å)
4511.0	57.76
4993.0	66.31
5502.0	52.36
5692.0	56.72
5792.0	65.63
5905.0	64.30
5988.5	51.19
6104.0	55.03
6190.0	51.60
6289.8	56.56
6380.0	58.36
6512.0	53.83
6585.0	73.64
6714.0	78.12
6809.0	74.29
6998.0	68.85
7312.0	70.00
7492.0	84.40
7791.0	54.32
8019.0	95.32
8206.0	68.63
8283.0	90.50
8490.0	50.71
8991.0	63.89

Table 2.2: The transmission curve data for the filter set

λ (Å)	Coeff	λ (Å)	Coeff	λ (Å)	Coeff	λ (Å)	Coeff	λ (Å)	Coeff	λ (Å)	Coeff
4420	0.000	4900	0.000	5400	0.000	5580	0.000	5710	0.000	5810	0.000
4430	0.013	4910	0.004	5410	0.004	5590	0.000	5720	0.013	5820	0.008
4440	0.040	4920	0.030	5420	0.018	5600	0.003	5730	0.047	5830	0.040
4450	0.088	4930	0.090	5430	0.058	5610	0.010	5740	0.194	5840	0.108
4460	0.200	4940	0.270	5440	0.130	5620	0.029	5750	0.480	5850	0.290
4470	0.365	4950	0.600	5450	0.230	5630	0.080	5760	0.563	5860	0.525
4480	0.450	4960	0.640	5460	0.357	5640	0.200	5770	0.539	5870	0.569
4490	0.473	4970	0.600	5470	0.450	5650	0.470	5780	0.550	5880	0.564
4500	0.475	4980	0.600	5480	0.500	5660	0.500	5790	0.574	5890	0.564
4510	0.475	4990	0.614	5490	0.515	5670	0.512	5800	0.570	5900	0.570
4520	0.472	5000	0.609	5500	0.525	5680	0.510	5810	0.520	5910	0.540
4530	0.472	5010	0.598	5510	0.500	5690	0.503	5820	0.508	5920	0.507
4540	0.472	5020	0.610	5520	0.480	5700	0.503	5830	0.530	5930	0.507
4550	0.461	5030	0.628	5530	0.450	5710	0.500	5840	0.540	5940	0.550
4560	0.420	5040	0.430	5540	0.400	5720	0.503	5850	0.445	5950	0.550
4570	0.370	5050	0.180	5550	0.266	5730	0.500	5860	0.250	5960	0.310
4580	0.250	5060	0.075	5560	0.165	5740	0.400	5870	0.115	5970	0.130
4590	0.135	5070	0.030	5570	0.093	5750	0.230	5880	0.056	5980	0.056
4600	0.070	5080	0.018	5580	0.047	5760	0.127	5890	0.030	5990	0.025
4610	0.040	5090	0.005	5590	0.024	5770	0.050	5900	0.020	6000	0.012
4620	0.020	5100	0.000	5600	0.010	5780	0.023	5910	0.012	6010	0.005
4630	0.009			5610	0.008	5790	0.011	5920	0.007	6020	0.000
4640	0.005			5620	0.004	5800	0.005	5930	0.000		
4650	0.001			5630	0.002	5810	0.003				
4660	0.000			5640	0.000	5820	0.000				

λ (Å)	Coeff	λ (Å)	Coeff	λ (Å)	Coeff	λ (Å)	Coeff	λ (Å)	Coeff	λ (Å)	Coeff
5880	0.000	6020	0.000	6100	0.000	6150	0.000	6290	0.000	6420	0.000
5890	0.003	6030	0.010	6110	0.017	6160	0.000	6300	0.010	6430	0.004
5900	0.008	6040	0.030	6120	0.060	6170	0.004	6310	0.044	6440	0.016
5910	0.011	6050	0.100	6130	0.230	6180	0.006	6320	0.135	6450	0.095
5920	0.030	6060	0.250	6140	0.385	6190	0.010	6330	0.375	6460	0.300
5930	0.075	6070	0.405	6150	0.410	6200	0.020	6340	0.557	6470	0.525
5940	0.228	6080	0.496	6160	0.433	6210	0.034	6350	0.578	6480	0.563
5950	0.450	6090	0.528	6170	0.490	6220	0.065	6360	0.567	6490	0.534
5960	0.515	6100	0.530	6180	0.519	6230	0.130	6370	0.553	6500	0.522
5970	0.510	6110	0.506	6190	0.493	6240	0.252	6380	0.502	6510	0.490
5980	0.495	6120	0.494	6200	0.474	6250	0.418	6390	0.452	6520	0.440
5990	0.505	6130	0.518	6210	0.500	6260	0.505	6400	0.448	6530	0.423
6000	0.520	6140	0.543	6220	0.571	6270	0.541	6410	0.500	6540	0.450
6010	0.525	6150	0.460	6230	0.375	6280	0.543	6420	0.551	6550	0.481
6020	0.490	6160	0.300	6240	0.130	6290	0.541	6430	0.340	6560	0.320
6030	0.400	6170	0.157	6250	0.043	6300	0.549	6440	0.140	6570	0.113
6040	0.235	6180	0.080	6260	0.019	6310	0.542	6450	0.050	6580	0.058
6050	0.075	6190	0.048	6270	0.009	6320	0.512	6460	0.020	6590	0.025
6060	0.026	6200	0.030	6280	0.002	6330	0.414	6470	0.010	6600	0.012
6070	0.010	6210	0.012	6290	0.000	6340	0.270	6480	0.004	6610	0.006
6080	0.005	6220	0.006			6350	0.154	6490	0.000	6620	0.003
6090	0.003	6230	0.000			6360	0.075			6630	0.003
6100	0.000					6370	0.032			6640	0.000
						6380	0.018				
						6390	0.011				
						6400	0.005				
						6410	0.004				
						6420	0.001				
						6430	0.000				

λ (Å)	Coeff	λ (Å)	Coeff	λ (Å)	Coeff	λ (Å)	Coeff	λ (Å)	Coeff	λ (Å)	Coeff
6460	0.000	6590	0.000	6700	0.000	6870	0.000	7160	0.000	7370	0.000
6470	0.005	6600	0.002	6710	0.004	6880	0.005	7170	0.002	7380	0.004
6480	0.020	6610	0.009	6720	0.012	6890	0.014	7180	0.010	7390	0.014
6490	0.060	6620	0.018	6730	0.042	6900	0.026	7190	0.017	7400	0.038
6500	0.160	6630	0.045	6740	0.100	6910	0.052	7200	0.028	7410	0.115
6510	0.365	6640	0.090	6750	0.220	6920	0.111	7210	0.042	7420	0.280
6520	0.490	6650	0.183	6760	0.358	6930	0.218	7220	0.065	7430	0.460
6530	0.544	6660	0.375	6770	0.470	6940	0.370	7230	0.108	7440	0.604
6540	0.564	6670	0.585	6780	0.530	6950	0.470	7240	0.160	7450	0.610
6550	0.592	6680	0.629	6790	0.585	6960	0.538	7250	0.265	7460	0.595
6560	0.600	6690	0.650	6800	0.628	6970	0.540	7260	0.395	7470	0.600
6570	0.604	6700	0.650	6810	0.635	6980	0.530	7270	0.485	7480	0.612
6580	0.591	6710	0.647	6820	0.620	6990	0.521	7280	0.505	7490	0.612
6590	0.586	6720	0.650	6830	0.594	7000	0.510	7290	0.505	7500	0.595
6600	0.602	6730	0.650	6840	0.594	7010	0.490	7300	0.500	7510	0.581
6610	0.584	6740	0.650	6850	0.602	7020	0.470	7310	0.508	7520	0.585
6620	0.456	6750	0.615	6860	0.550	7030	0.455	7320	0.525	7530	0.601
6630	0.250	6760	0.550	6870	0.390	7040	0.455	7330	0.534	7540	0.560
6640	0.140	6770	0.410	6880	0.220	7050	0.423	7340	0.520	7550	0.460
6650	0.070	6780	0.215	6890	0.113	7060	0.330	7350	0.490	7560	0.246
6660	0.036	6790	0.100	6900	0.070	7070	0.190	7360	0.451	7570	0.112
6670	0.020	6800	0.048	6910	0.039	7080	0.095	7370	0.382	7580	0.070
6680	0.011	6810	0.022	6920	0.023	7090	0.040	7380	0.250	7590	0.039
6690	0.007	6820	0.011	6930	0.015	7100	0.018	7390	0.133	7600	0.023
6700	0.004	6830	0.005	6940	0.010	7110	0.010	7400	0.066	7610	0.013
6710	0.003	6840	0.002	6950	0.005	7120	0.004	7410	0.029	7620	0.009
6720	0.000	6850	0.001	6960	0.000	7130	0.000	7420	0.014	7630	0.002
		6860	0.000					7430	0.006	7640	0.000
								7440	0.004		
								7450	0.001		
								7460	0.000		

λ (Å)	Coeff	λ (Å)	Coeff	λ (Å)	Coeff	λ (Å)	Coeff	λ (Å)	Coeff	λ (Å)	Coeff
7670	0.000	7810	0.000	8080	0.000	8120	0.000	8340	0.000	8840	0.000
7680	0.004	7820	0.000	8090	0.005	8130	0.002	8350	0.005	8850	0.003
7690	0.009	7830	0.004	8100	0.012	8140	0.010	8360	0.005	8860	0.005
7700	0.018	7840	0.004	8110	0.018	8150	0.012	8370	0.007	8870	0.010
7710	0.037	7850	0.010	8120	0.035	8160	0.021	8380	0.010	8880	0.015
7720	0.070	7860	0.015	8130	0.070	8170	0.030	8390	0.018	8890	0.025
7730	0.140	7870	0.020	8140	0.130	8180	0.050	8400	0.021	8900	0.035
7740	0.252	7880	0.030	8150	0.240	8190	0.078	8410	0.040	8910	0.060
7750	0.410	7890	0.045	8160	0.383	8200	0.115	8420	0.070	8920	0.095
7760	0.500	7900	0.063	8170	0.511	8210	0.177	8430	0.130	8930	0.150
7770	0.520	7910	0.098	8180	0.583	8220	0.240	8440	0.225	8940	0.225
7780	0.507	7920	0.140	8190	0.620	8230	0.330	8450	0.350	8950	0.315
7790	0.497	7930	0.190	8200	0.623	8240	0.439	8460	0.430	8960	0.419
7800	0.499	7940	0.267	8210	0.623	8250	0.520	8470	0.500	8970	0.495
7810	0.502	7950	0.370	8220	0.626	8260	0.565	8480	0.513	8980	0.535
7820	0.450	7960	0.480	8230	0.626	8270	0.611	8490	0.474	8990	0.555
7830	0.330	7970	0.535	8240	0.555	8280	0.635	8500	0.430	9000	0.564
7840	0.235	7980	0.580	8250	0.416	8290	0.645	8510	0.400	9010	0.572
7850	0.160	7990	0.610	8260	0.310	8300	0.650	8520	0.350	9020	0.568
7860	0.100	8000	0.618	8270	0.200	8310	0.650	8530	0.310	9030	0.536
7870	0.060	8010	0.618	8280	0.116	8320	0.635	8540	0.248	9040	0.410
7880	0.043	8020	0.610	8290	0.065	8330	0.590	8550	0.190	9050	0.290
7890	0.030	8030	0.600	8300	0.040	8340	0.520	8560	0.125	9060	0.196
7900	0.022	8040	0.585	8310	0.022	8350	0.430	8570	0.085	9070	0.121
7910	0.016	8050	0.560	8320	0.016	8360	0.314	8580	0.050	9080	0.071
7920	0.012	8060	0.515	8330	0.009	8370	0.220	8590	0.033	9090	0.042
7930	0.006	8070	0.440	8340	0.006	8380	0.164	8600	0.022	9100	0.027
7940	0.003	8080	0.370	8350	0.003	8390	0.117	8610	0.014	9110	0.018
7950	0.000	8090	0.291	8360	0.000	8400	0.080	8620	0.010	9120	0.012
		8100	0.222			8410	0.056	8630	0.006	9130	0.008
		8110	0.164			8420	0.045	8640	0.000	9140	0.006
		8120	0.117			8430	0.031			9150	0.003
		8130	0.088			8440	0.024			9160	0.002
		8140	0.070			8450	0.018			9170	0.001
		8150	0.049			8460	0.011			9180	0.000
		8160	0.040			8470	0.010				
		8170	0.028			8480	0.005				
		8180	0.024			8490	0.000				
		8190	0.018								
		8200	0.014								
		8210	0.010								
		8220	0.008								
		8230	0.005								
		8240	0.004								
		8250	0.003								
		8260	0.000								
		8270	0.000								

2.2 Observations

CCD images were obtained at the Canada-France-Hawaii Telescope by P. Hickson and H. Yee on the nights of February 14/15 through 17/18, 1988. The UBC focal reducer (Hickson, Richardson, and Grundmann 1992) was used at the f/8 Cassegrain focus, for a focal ratio of f/2.5. The detector was the RCA4 chip, and the total field size was approximately 3.7×6 arcminutes, with a pixel size of 0.344 arcseconds. Seeing over the four nights ranged from 0.9 to 1.3 arcsec. The observers recorded cirrus at the horizon in the morning following the second night. The two hours prior to their noticing the presence of cirrus had been spent taking dome flat field observations, so an unknown degree of extinction may or may not have affected the night's observations in the filters at central wavelengths 4500Å, 5700Å, 5900Å, 6000Å, 6200Å, 8000Å, 8200Å, and 8300Å. The possibility of calibration error is dealt with as discussed in section 4.5.

Two standard stars were observed in order to calibrate the photometry (section 3.2). The stars were HD19445 and HD84937, from Oke and Gunn's (1983) list of subdwarf standards. Exposure times were one or two seconds. HD19445 was observed at least once in all the filters and twice in four of them, while HD84937 was observed in only four filters. (See the table of zero points in section 3.2.1.)

On the cluster fields, exposure times were 300 to 1800 seconds, depending on the filter wavelength. Night sky emission-line interference fringes were visible in the cluster images taken in the 8300Å filter. Normally this signal would be removed by dividing the data by a "fringe frame", a median of all the data frames showing the fringes. However, there were only four images, two of the 3C281 field and two of the field around the quasar PKS0812+020, which showed the fringing signal, and the median image of these four still retained artifacts of the objects in the fields. Since this would have seriously affected the

photometry, no correction was made to the image. The effect of the fringing is discussed further in the section dealing with uncertainties, 3.3.

The sources in the cluster frames show significant coma near the edges of the images. The effect of the coma is to spread the light from the object over a larger area than it would cover at the centre of the frame. The peak brightness and the signal-to-noise ratio are therefore reduced, as more light is lost to the faint edges of the image. As a result less light is measured in any given aperture than would be detected in the absence of the distortion, and the object appears fainter than it should.

2.3 Basic Reductions and Object-Finding

The IRAF package[2] was used for the initial reduction of the data. Median biases were constructed for each night, and the images were bias-subtracted, flat-fielded using dome flats, and trimmed of the overscan region.

The images were converted from real to short integer pixels and read into H. Yee's aperture-photometry program, PPP (described in chapter 3 and more fully in Yee 1990). The positions of reference objects in the field were used to align and trim the images, so that a given object would lie at the same coordinates in every frame.

Object detection was performed on median images of the field. These were constructed by scaling the background levels of an image in each of the twenty-four filters to the same value, and then taking the median value for each pixel. Because two observations of the field were made in every filter, two independent median images were made. In such an image, the sky background is smoothed out, improving the signal-to-noise and visibility

[2]IRAF is distributed by the National Optical Astronomy Observatories, which is operated by the Association of Universities for Research in Astronomy, Inc., under contract to the National Science Foundation.

of real objects in the field.

The object-finding routine in PPP is a modified version of that used by Kron (1980). When a local maximum is found, a flux is measured from the central nine pixels around the maximum, and a local sky, computed as the mode of the pixel values in an annulus of inner and outer radii five and eleven pixels, is subtracted. If the "object flux" lies above a given threshold, then the position of the maximum is recorded as a detection. If the threshold is set low enough to detect faint and diffuse objects, a number of noise detections will also be made. Cross-checking the detection lists from the two independent images, and eliminating detections not seen on both frames (within two pixels of the position), removes most, although not all, of the noise-spike detections.

The threshold level for object detection was selected to be 1.2 times the standard deviation of the sky background pixels across the frame. Object-finding was done at various threshold levels, from 0.8σ to 2σ, and it was found that after cross-checking the two object lists, the number of detections did not increase substantially below a threshold level of 1.2σ. Such a threshold is low for putting confidence in real detections, but helps avoid missing objects which might be bright only in some filters. (The median image of such objects could be quite low in intensity.) The signal-to-noise value for every object in each filter was later computed, and the median of these values taken as a representative signal-to-noise for the detection (section 4.6).

The cross-checked list was visually compared with both median images. Detections were removed from the list if they were obviously due to chance alignment of noise spikes, or if they lay in the haloes of relatively large galaxy images. The object-finding routine occasionally missed extended diffuse objects. If evidence could be seen for an object in both sum frames, the object was added to the list. After this, the preliminary list contained 184 detections.

Chapter 3

Photometry

Galaxy photometry can be approached in a variety of ways. Some methods involve the fitting of elliptical profiles, with a range of eccentricities and angles of rotation, to galaxy images. Others measure the light within an aperture of fixed size, or attempt to select an aperture of appropriate size for each object. Because the object images in this study were not large or well-resolved enough to allow profile-fitting, the applicability of the latter two techniques was studied.

3.1 Aperture Photometry

Photometry of the objects in this field went through several incarnations. The first method tested was growth-curve aperture photometry. Light from an object is measured in a series of concentric circular apertures. The resulting "growth curve" is analyzed to determine the size of the object and hence the appropriate aperture. For example, the growth curve of a relatively compact, isolated object will stop rising when the aperture is larger than the object; the aperture at which this occurs is selected as the appropriate one for photometry of the object. [1] Any error in the calculated sky level will cause the

[1]This is not necessarily the aperture in which the signal-to-noise ratio is maximized; an alternative technique employs that method, but it was not tested on this data set.

growth curve to turn up or down in the apertures where little light from the object is detected. The aperture prior to the drop (if the sky is overestimated) or to the upturn (if underestimated) is identified as the best one to use.

A disadvantage of the growth-curve technique for aperture selection is that it may tend to underestimate the brightness of an extended isolated object. This is due to the "termination condition" of setting the aperture just inside a perceived drop in flux, because the possibility is not considered that noise superimposed on the object may cause the growth curve to fluctuate both up and down. In this way, a significant amount of signal from the outer regions of the object can be lost, especially for faint or diffuse objects whose outer regions will be badly affected by noise. This is also a problem for objects that might lie close to low-valued columns or pixels. The growth-curve technique, as described here, can therefore introduce a bias in the flux measurements.

The potential bias from the growth-curve method could have a serious effect on spectral energy distributions composed of multi-filter data, since the difference between fluxes in adjacent filters can be crucial in later determining object type and redshift. For that reason, a fixed-aperture approach was chosen for the photometry.

H. Yee's photometry program PPP was used to compute the total flux in a set of apertures with diameters up to thirty-five pixels (where the pixel size is 0.344 arcseconds). The background sky level is calculated with the modal sky estimator, $3\times median - 2\times mean$, where the mean and the median are computed, with an iterative outlier rejection algorithm, in an annulus surrounding the object and the largest object aperture.

The flux for each object in each filter was taken from an aperture of diameter approximately twice the full width at half maximum, seven pixels or 2.4 arcseconds across. The light within this aperture represents the light from the whole object, without the complications introduced by estimating a size for the object in each filter image.

The spectral energy distributions produced later are compared with model galaxy spectra. Because the model spectra of spiral galaxies are composed of separate bulge and disk components, it is important to be sure that spiral arms as well as central bulges fall within the aperture so that spirals will not be misclassified as ellipticals. The angular size–redshift relation (e.g. as in Sandage 1988, page 610) allows the calculation of the linear size d at a given redshift corresponding to the angular size of the aperture. For example, for a universe with $q_o = \frac{1}{2}$, $d = 1.6/h_{100}$ kpc at $z = 0.05$, $d = 3.0/h_{100}$ kpc at $z = 0.1$, and at $z = 0.2$, $d = 5.0/h_{100}$ kpc. A galaxy for which identification might be a problem, then, would be a face-on spiral at low redshift, especially if $H_o = 100$ km/s/Mpc. However, at redshifts above 0.1 or 0.2, there should be no such confusion, so use of an aperture this size seems reasonable.

3.2 Calibration

The conversion from instrumental (PPP) magnitudes to real intensity units was made using the following calibration equation :

$$m = m_{PPP} + 2.5 \log \tau + A_0 + EX$$

where

m is $-2.5 \log f$, where f is the total flux in ergs s^{-1} cm^{-2} through the filter,

$m_{PPP} + 2.5 \log \tau$ is the magnitude based on flux from a one-second exposure,

m_{PPP} is the magnitude given by PPP,

τ is the exposure time,

A_0 is the zero point for the calibration,

X is the airmass, and

E is the extinction at the filter wavelength, which is from the "Mauna Kea Extinction

Curve", figure [5]-3a in the 1990 CFHT Users' Manual.

No colour term was included in the equation because the colours of the standard stars were not sufficiently different for a solution to be found. If the colour term is significant, it could introduce errors in the calibration.

3.2.1 Zero Points

Two standard stars from Oke and Gunn (1983) were used to determine the zero point for the calibration of each filter. Oke and Gunn give spectral energy distributions over the range 3080Å to 12000Å for a set of subdwarf standards in AB_{79} magnitudes. These were converted into flux units of ergs s^{-1} cm^{-2} Hz^{-1} by the equation [2]

$$AB_{79} = -2.5 \log f_\nu - 48.60.$$

The filter transmission curves provided by the manufacturer were sampled every ten ångstroms. The flux through each filter was computed by summing the product of the filter transmission coefficient T times f_ν multiplied by the sampling width in Hertz, effectively evaluating the integral $\int T f_\nu d\nu$ over the filter. The resulting flux, f, was substituted into the calibration equation, along with the PPP magnitude for the star in that filter, exposure time, extinction coefficient and airmass, and the zero point was calculated.

For those four filters in which both standard stars were observed, the difference in zero points derived from the two stars was on the order of 0.04 magnitudes. This is a measure of the uncertainty in the derivation of the zero point; it does not represent a night-to-night variation in the value because all observations in a given filter were made on the same night. Table 3.1 lists all the zero points derived in these filters. The table also lists the derived uncertainties in the zero point, which include uncertainty in Oke

[2]The sign of the constant in this equation is different from that given by Oke and Gunn. The change is justified by noting that absolute flux from a star of apparent magnitude V=0.000 at 5480 Å is 3.65×10^{-20} ergs s^{-1} cm^{-2} Hz^{-1} (Oke & Schild 1970), and that $AB_{79} \equiv V$ at 5480 Å.

and Gunn's spectral energy distribution for the standard as well as uncertainty in the flux measured from the image. Calculation of these values is described in section 3.3.1.

3.2.2 Spectral Energy Distributions

The measured magnitude of each object was converted to a true magnitude by the calibration equation, using the airmass from the middle of the exposure for the best approximation. Estimates of the uncertainties in the contributing quantities are described in section 3.3.

In the case that PPP was unable to calculate an object magnitude in a given filter because background subtraction left a negative flux value, the flux was set to zero. Such data points were excluded from the later SED-fitting procedure.

A list was then compiled with one object spectral energy distribution per line. This consisted of the object number and position in the field, followed by the intensity and its uncertainty for each filter, ordered by central wavelength. Fluxes in this list were recorded in units ergs s^{-1} cm^{-2} so as to be compatible with the model-fitting program. However, the data displayed later (section 4.4) are shown in the form $log f_\lambda (ergs\, s^{-1} cm^{-2} \mathring{A}^{-1}$ vs. λ.

3.3 Uncertainty Estimates

The uncertainty estimate for the points is of great importance, since these uncertainties appear in the χ^2 function which is minimized to determine the template which best fits the object spectral energy distribution. Uncertainties arise in every term of the calibration equation, in the zero point itself, and in external influences on the data such as galactic extinction and interference fringes.

Table 3.1: Table of the zero point values derived from all the observations of standard stars in these filters. There were multiple standard observations in only four filters.

Filter λ	HD19445 Obsn 1	HD19445 Obsn 2	HD84937 Obsn 1
4511	37.632 ± 0.040		
4993	38.101 ± 0.029		
5502	37.474 ± 0.044		
5692	37.310 ± 0.039		
5792	37.512 ± 0.033		
5905	37.662 ± 0.031		
5989	37.520 ± 0.041		
6104	37.605 ± 0.037		
6190	37.547 ± 0.035		
6290	37.616 ± 0.046	37.609	37.658
6380	37.661 ± 0.033	37.631	37.673
6512	37.594 ± 0.039	37.573	37.629
6585	37.574 ± 0.035		
6714	37.501 ± 0.033		
6809	37.574 ± 0.034		
6998	38.448 ± 0.037		
7312	37.556 ± 0.042		
7492	38.037 ± 0.031		
7791	37.224 ± 0.050		
8019	37.691 ± 0.045		
8206	37.064 ± 0.040		
8283	36.987 ± 0.040		
8490	37.912 ± 0.057	37.917	37.911
8991	37.386 ± 0.052		

3.3.1 Zero Point Uncertainty

An estimate of the zero-point uncertainty is made by considering each term of the calibration equation in turn :

$$A_0 = m_{AB} - m_{PPP} - 2.5 \log \tau - EX.$$

To estimate the uncertainty in the "true magnitude" of the standard, the 0.01-magnitude error bar in Oke and Gunn's SED measurements is considered. The filter transmission curve is sampled every 10 Å, so at each of these sample points, a Δf_ν is computed from

$$\Delta f_\nu = \frac{1}{2}\left[10^{\frac{(m+48.60)-\Delta m}{-2.5}} - 10^{\frac{(m+48.60)+\Delta m}{-2.5}}\right]$$

This quantity is multiplied by the sample width (i.e. 10 Å) in Hertz, and summed over the width of the filter.

The uncertainty in m_{PPP} is primarily ascribed to the level of sky noise in the aperture; this will dominate the counts for the faint objects, at least. Yee (1991) calculates this uncertainty ΔF for an object with F counts in the aperture as the product $\Delta F = \sigma_{sky}\sqrt{N_{pix}}$, where σ_{sky} is the rms value per pixel in the local sky, and N_{pix} is the total number of pixels in the aperture. The local sky is the mode of the pixel values in an annulus with inner diameter 35 pixels and outer diameter 73 pixels. The area of the annulus is large enough to represent a reasonable statistical sampling of the sky around the object. The "signal-to-noise" calculated by PPP's photometry routine is the value $\frac{F}{\Delta F}$, and hence ΔF can be computed in flux units (ergs s^{-1} cm^{-2}) by taking F as the true flux calculated from the SED.

The square root of the number of photons detected from the object is a further source of error for the bright standard stars, although it is completely dominated by the sky noise in faint objects.

The exposure time τ is very short (either one or two seconds) for the standard stars. This time may be in error by as much as five per cent (H. Richer, pers. comm.), due to the finite time taken for the shutter to close. The error due to this factor could not be estimated because no longer exposure of a standard was taken.

Because the change in zenith distance over the exposure time is almost infinitesimal, no error is assumed in the airmass X. The differential atmospheric extinction was obtained from the graph of mean extinction for the site published in the CFHT *Users' Manual.* Unfortunately the manual does not quote the typical night-to-night variation in the extinction, nor can it be estimated from the data, since repeated observations of standards on different nights in the same filters were not made. The uncertainty in reading the values from the curve is taken as ± 0.003 magnitudes per airmass.

The total uncertainty in A_0 is computed by the method of partial derivatives, as described by Bevington (1969, Chapter 4). The uncertainties in the terms of the calibration equation are assumed to be uncorrelated, and therefore no cross terms are included in the error calculation.

The calibration equation is rewritten in the form

$$A_0 = -2.5 \log f + 2.5 \log C - 2.5 \log \tau - EX$$

where f is the calibrated flux and C is the number of counts representing the object brightness. Then the zero-point uncertainty σ_{A_0} is given by :

$$\sigma_{A_0}^2 = \sigma_f^2 \left(\frac{\partial A_0}{\partial f}\right)^2 + \sigma_C^2 \left(\frac{\partial A_0}{\partial C}\right)^2 + \sigma_\tau^2 \left(\frac{\partial A_0}{\partial \tau}\right)^2 + \sigma_E^2 \left(\frac{\partial A_0}{\partial E}\right)^2 + \sigma_X^2 \left(\frac{\partial A_0}{\partial X}\right)^2$$

where σ_τ and σ_X are zero for the standard star observations.

Substituting for the partial derivatives, and including the appropriate values for the uncertainties σ, yields the zero point uncertainty. Since the number of photons counted

for a star, after sky subtraction, is the sum of the contribution from the star itself and the contribution from sky noise, the partial derivative analysis gives

$$\sigma_C = \sqrt{\sigma^2_{C_{obj}} + \sigma^2_{C_{sky-noise}} + \sigma^2_{C_{sky-subtr}}}$$

and the zero point error is

$$\sigma^2_{A_0} = (2.5 \log e)^2 \left[\left(\frac{\sigma_{I_c}}{I_c} \right)^2 + \left(\frac{\sigma_C}{C} \right)^2 \right] + \sigma^2_E X^2.$$

3.3.2 Calibration Uncertainty

Sources of uncertainty in the calibration other than those from the zero point include the contribution from sky noise in the aperture (as discussed in section 3.3.1), the contribution from atmospheric extinction, and that from the airmass. The other sources of uncertainty in the derived magnitudes originate in galactic extinction and the presence of sky emission interference fringes in some of the data frames.

A mid-exposure airmass was used in the calibration equation. The uncertainty in this quantity is the difference between the mid-exposure airmass and the average airmass over the exposure. For twenty-minute exposure times and fields near the meridian, the contribution of the airmass to the uncertainty was taken to be so small that it was not included in the error calculation.

The colours of the galaxies in the field, as compared to model galaxy spectra, may be affected somewhat by galactic absorption, although the quasar is at a high galactic latitude : $\ell = 314.50°, b = 69.20°$ (epoch 1950). An analytical calculation was made to estimate the effect of galactic absorption in the the filter bandpasses using a typical hydrogen density for the galaxy [3] and an extinction formula from Lang (1986, p. 565). The

[3] Mihalas and Binney (1981) describe the most common constituents of the ISM as (1) hot neutral gas surrounding cool clouds, occupying 20% of the volume and having number density 0.3 cm^{-3}, and (2)

amount of absorption through 100 pc was found to be on the order of 0.036 magnitudes for the reddest filter and 0.02 for the bluest. Since the true nature of the interstellar medium in the direction of the cluster is not included in this calculation, these values cannot be used as a correction, but they are taken as representative of the uncertainty in the object magnitude due to galactic absorption. The appropriate value was included in the total uncertainty for each object in each filter.

Although the estimated uncertainties due to extinction quoted above were applied to the flux uncertainty in the data used for the project, a more appropriate course of action would be to make an extinction correction in each filter based on the column density along the line of sight to the field. Burstein and Heiles (1978) published column densities and reddenings for three objects within about 20 degrees of the 3C281 field. The E(B-V) values they listed for the objects (0.03, 0.00, and -0.02, with an estimated uncertainty of 0.03) yield maximum extinction values by the method of Cardelli, Clayton, and Mathis (1989) of about 0.003 at the red end of the filter set and 0.057 at the blue end. Given the errors in the measured reddening, the uncertainties applied to the flux data are not unreasonable, although a correction to the flux would have been better.

Interference fringe patterns were observed in the 8300Å filter images. They were probably due to an atmospheric emission line near this wavelength entering the filter. An attempt was made to create a fringe pattern image which could then be removed from the data. Because there were only four images showing the fringe pattern, however, it proved impossible to successfully remove the fringes without seriously affecting the quality of the object images. It was not thought necessary to add an extra error term to describe the effect of the fringing on the photometry, because the fringing occurs on a small enough

hot, low-density gas, occupying 70% of the volume and with number density 10^{-3} cm^{-3}. The hydrogen number density of the former was used in the extinction estimate, although areas of the galaxy containing clouds will have higher densities.

scale (about twenty pixels) that it is perceived as a further source of sky noise in the local sky aperture. Its effect is therefore included in the signal-to-sky-noise ratio calculated by PPP.

As was done for the zero-point error, the uncertainty in the photometry is propagated using the method of partial derivatives. This time, however, the uncertainty is needed in the linear domain (intensity units), so the calibration equation is rewritten as

$$f = \frac{C}{\tau}\, 10^{-0.4(EX+A_0)}$$

where the variables are as defined above in section 3.3.1.

The total uncertainty σ_f in the calibrated intensity derived for an object is given by

$$\left(\frac{\sigma_f}{f}\right)^2 = \left(\frac{1}{S/N}\right)^2 + \left(\frac{\ln 10}{-2.5}\right)^2 E^2\,\sigma_X^2 + \left(\frac{\ln 10}{-2.5}\right)^2 \sigma_E^2 X^2 + \left(\frac{\ln 10}{-2.5}\right)^2 \sigma_{A_0}^2.$$

The term representing the square root of the number of photons received from the object has been left out of the equation above, since it is generally overwhelmed by the sky noise for the faint objects.

The value $flux/uncertainty$, or $\frac{f}{\sigma_f}$, is a measure of signal-to-noise ratio in the aperture.

Chapter 4

Redshifts and Type Classification

4.1 Overview

The classification of the field objects based on the nature of their spectral energy distributions (SEDs) is accomplished by the brute-force method of making a quantitative comparison between the observed SED and each one of an array of artificial SEDs, produced by multiplying the filter transmission curves by a set of galaxy and star fiducial spectra.

The galaxy model SEDs, or templates, are calculated over a range of redshifts, from zero to one in increments of 0.005 in log(1+z). This corresponds to an effective resolution in redshift of from 0.01 to 0.02. Each model SED is multiplied by a scale factor which minimizes χ^2, based on the ratio of the raw model intensity to the data intensity. Then the goodness of the model fit is quantified by calculating a reduced χ^2 value:

$$\chi^2 = \frac{1}{\nu} \sum_{i=1}^{no.filters} \frac{(f_i^{model} - f_i^{data})^2}{\sigma_i^2}$$

where ν is the number of filters defining the SED, and σ is the uncertainty in the intensity of the data point (as discussed in section 3.3). The model yielding the lowest χ^2 value is understood to best represent the physical nature and redshift (for galaxies) of the object.

It should be noted that this χ^2 does not have the usual statistical meaning. The

quantity ν represents the number of degrees of freedom and is taken as the number of filters, but the filters overlap and are therefore not completely independent. The χ^2 calculated here is useful for comparing the fits of models to a single data set (i.e. the SED for a single object), but cannot be used to estimate the statistical significance of a fit, and cannot even be compared between fits to different data sets.

A further problem with the χ^2 value is related to the uncertainties σ_i. For a useful statistical χ^2 value, the errors must be uncorrelated and have a gaussian distribution. However, the errors in each filter are primarily dependent on the sky noise in the image, which varies significantly for observations in different filters. The uncertainties in a given SED are therefore unlikely to be gaussian in distribution.

The fiducial spectra available represent a sequence of normal galaxies and stars. Any objects with spectra not included in this sequence, such as emission-line galaxies and QSOs for example, cannot be recognized as such without visual inspection. The best-fitting model is assigned; if the uncertainties were well understood and the filters independent, the value of the χ^2 would illustrate how close the best-fit model is to the real SED. Such an estimate of goodness-of-fit would be valuable in determining confidence in the derived object type and redshift.

The following sections describe the sets of fiducial spectra, then some of the details and complications of the fitting procedure, and finally the results of applying the fitting program to the real data from the 3C281 field.

4.2 The Templates

P. Hickson's fitting program compares spectral energy distributions of the objects in the fields with SEDs constructed from fiducial star and galaxy spectra in the literature. The eighty-one star spectra, from Gunn and Stryker's (1983) stellar atlas, range from

type O5 to M8III and M8V. The galaxy templates are taken from Rocca-Volmerange and Guiderdoni's (1988) atlas of synthetic spectra, which consists of eight morphological types of galaxies, evolved to twenty ages from 0.08 Gyr to 19.08 Gyr using the galaxy spectrophotometric evolution package [1] of Guiderdoni and Rocca-Volmerange (1987). The seven types used for template-fitting in this study range from E/S0 through the spirals to an Ir galaxy. Intermediate templates are produced by linearly interpolating between spectra of successive types. Table 4.1 lists the galaxy and star types in the set of templates, together with their reference numbers.

While the fitting program is able to fit galaxy templates of varying ages, the data are not of high enough quality to justify introducing the "spectral age" of the galaxy as a separate parameter. The appropriate age for the galaxy templates should correspond to the model spectra which are likely to match the largest number of galaxies in the observed field. The most significant change with time in the spectrum of a galaxy occurs early in its life; after about twelve to fourteen gigayears of evolution, the spectrum does not alter much more, as demonstrated by figure 4.1. This data set is unlikely to reach deep enough to see galaxies early in their formation, so young galaxy templates were not considered. The 12.08–Gyr templates were adopted for fitting to the entire sample. Figure 4.2 shows this set of templates at zero redshift.

4.3 Details of the Fitting Process

The points in the model galaxy templates represent the flux that would be measured in each filter for a galaxy of the model type and redshift. Each point is the sum over the

[1]This package assumes solar metallicity and does not take chemical evolution into account. However, no models currently available do otherwise. At any rate, errors due to this assumption will occur primarily in the blue end of the spectrum, and will not be important in the spectral range observed for most of the galaxies in this study.

Table 4.1: Key to the numerical classifications used to refer to galaxy and star types.

Galaxies	
0 = cold E0	1 = hot E0
2 = Sa	3 = Sb
4 = Sc	5 = Sd
6 = Im	

Stars			
0 = O5	1 = O6	2 = O8V	3 = B0Ib
4 = B1IV	5 = B1	6 = B2III	7 = B2V
8 = B3III	9 = B3IV	10 = B3V	11 = B4V
12 = B5Ib	13 = B6V	14 = B7III	15 = B7IV
16 = B7V	17 = B8Ia	18 = B9IV	19 = B9V
20 = A0IV	21 = A0V	22 = A1V	23 = A2V
24 = A3III	25 = A3IV	26 = A3V	27 = A4IV
28 = A5III	29 = A5IV	30 = A5V	31 = A7V
32 = A9IV	33 = F0IV	34 = F2IV	35 = F4V
36 = F5IV	37 = F6V	38 = F7IV	39 = F8V
40 = F9V	41 = G0V	42 = G2IV	43 = G2V
44 = G3IV	45 = G4IV	46 = G5IV	47 = G5V
48 = G6IV	49 = G7IV	50 = G8III	51 = G8IV
52 = G8V	53 = K0III	54 = K0IV	55 = K0V
56 = K1III	57 = K1IV	58 = K2III	59 = K2IV
60 = K3III	61 = K3V	62 = K4III	63 = K4V
64 = K5III	65 = K7V	66 = K8V	67 = M0III
68 = M0V	69 = M1III	70 = M2III	71 = M2V
72 = M3III	73 = M4V	74 = M5III	75 = M5V
76 = M6III	77 = M6V	78 = M7III	79 = M8III
80 = M8V			

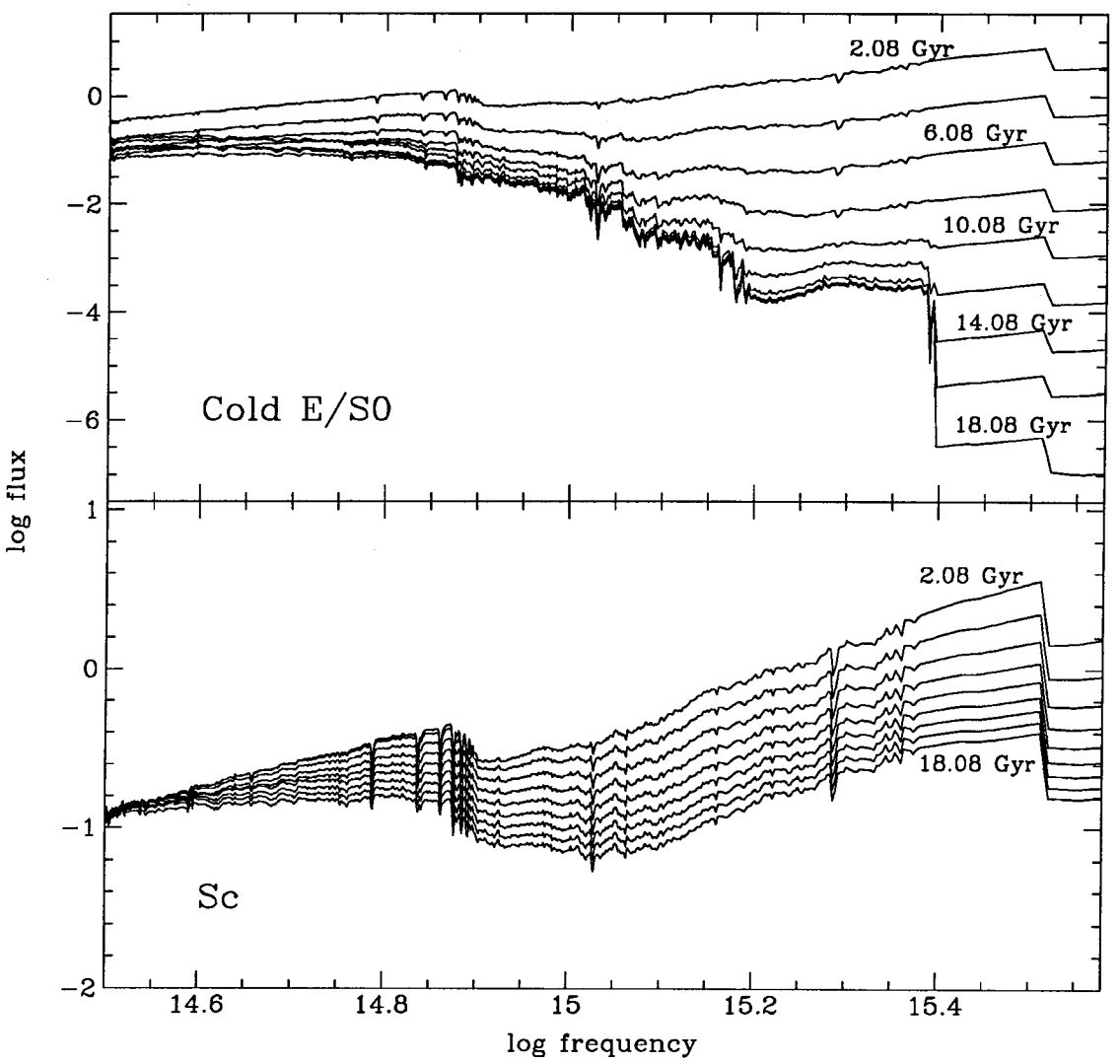

Figure 4.1: The change in a zero-redshift galaxy spectrum with age. The upper window shows evolution of a model UV-cold E/S0 spectrum (Rocca-Volmerange and Guiderdoni 1988) from age 2.08 Gyr to 18.08 Gyr, while the lower figure shows the same for a spiral galaxy. The vertical axis is in units $5.32 \times 10^{29} ergs\ s^{-1}\ \mathring{A}^{-1}\ M_{\odot}^{-1}$. Notice the difference in the vertical scales of the two plots. The shape of a galaxy spectrum changes less as the galaxy ages.

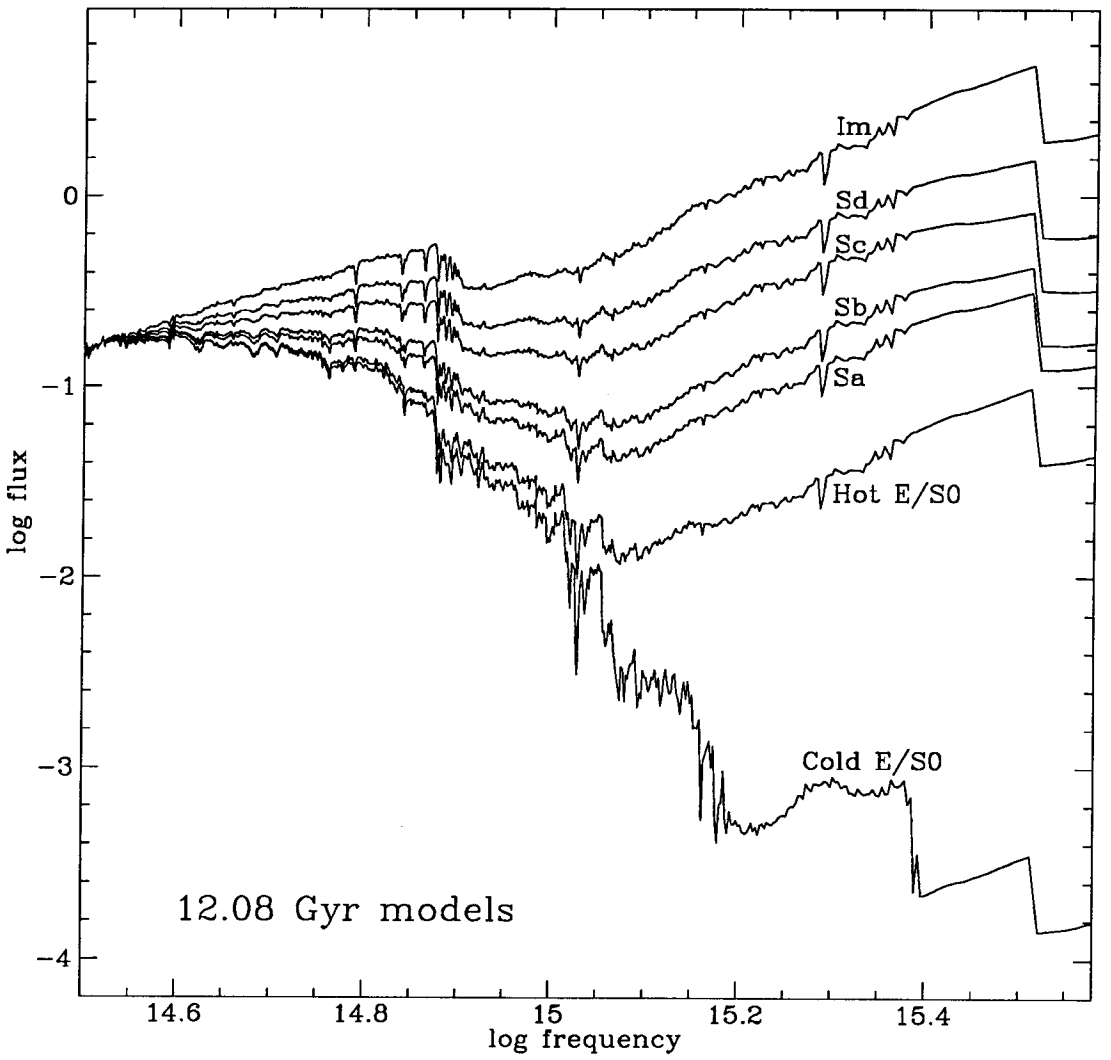

Figure 4.2: The model galaxy spectra (from Rocca-Volmerange and Guiderdoni 1988) at age 12.08 Gyr and zero redshift. These spectra are used as the fiducials in the template-fitting program and have been scaled to the same level at 5500 Å. In this figure the spectra have been slightly offset from one another so that they can be more clearly seen at the lower-frequency end.

filter transmission curve of the quantity

$$T_i f_{\nu_i}(z) \Delta \log \nu_i$$

where T_i is the i^{th} transmission coefficient of the filter, $f_{\nu_i}(z)$ is the redshifted model galaxy flux (in W Hz^{-1} $M_\odot^{-1}$) at the filter sample frequency, and $\Delta \log \nu_i = 0.001$ is the separation between samples in log frequency space.

Model SEDs are computed for galaxy redshifts from zero to one, in increments of 0.005 in log(1+z). For an elliptical galaxy, the change in spectral shape with redshift is quite dramatic, a fact made use of by Koo (1985) and others who used optical colours to deduce large numbers of redshifts. However, later-type galaxies have flatter spectra and smaller 4000-Å breaks, and as figure 4.3 demonstrates, it is much more difficult to assign an accurate redshift to a given SED. Erratic SED data points due to noise and errors in the photometry can make it still harder to discern the redshift.

The model SEDs must be multiplied by some scale factor before they can be quantitatively compared with the real SED. This scale factor is computed by equating to zero the first derivative, with respect to the scale S, of the reduced χ^2 formula

$$\chi^2 = \frac{1}{\nu} \sum_{i=1}^{no.filters} \frac{(f_i^{obj} - S \times f_i^{model})^2}{{\sigma_i}^2}.$$

The resulting scale, representing the minimum χ^2, is

$$S = \frac{\sum_{i=1}^{no.filters} f_i^{obj} f_i^{model} / \sigma_i^2}{\sum_{i=1}^{no.filters} {f_i^{obj}}^2 / \sigma_i^2}.$$

The effect of the σ in the denominators of the two quantities is to weight the scale value towards the value of f^{obj}/f^{model} where f^{obj} has the smallest uncertainty.

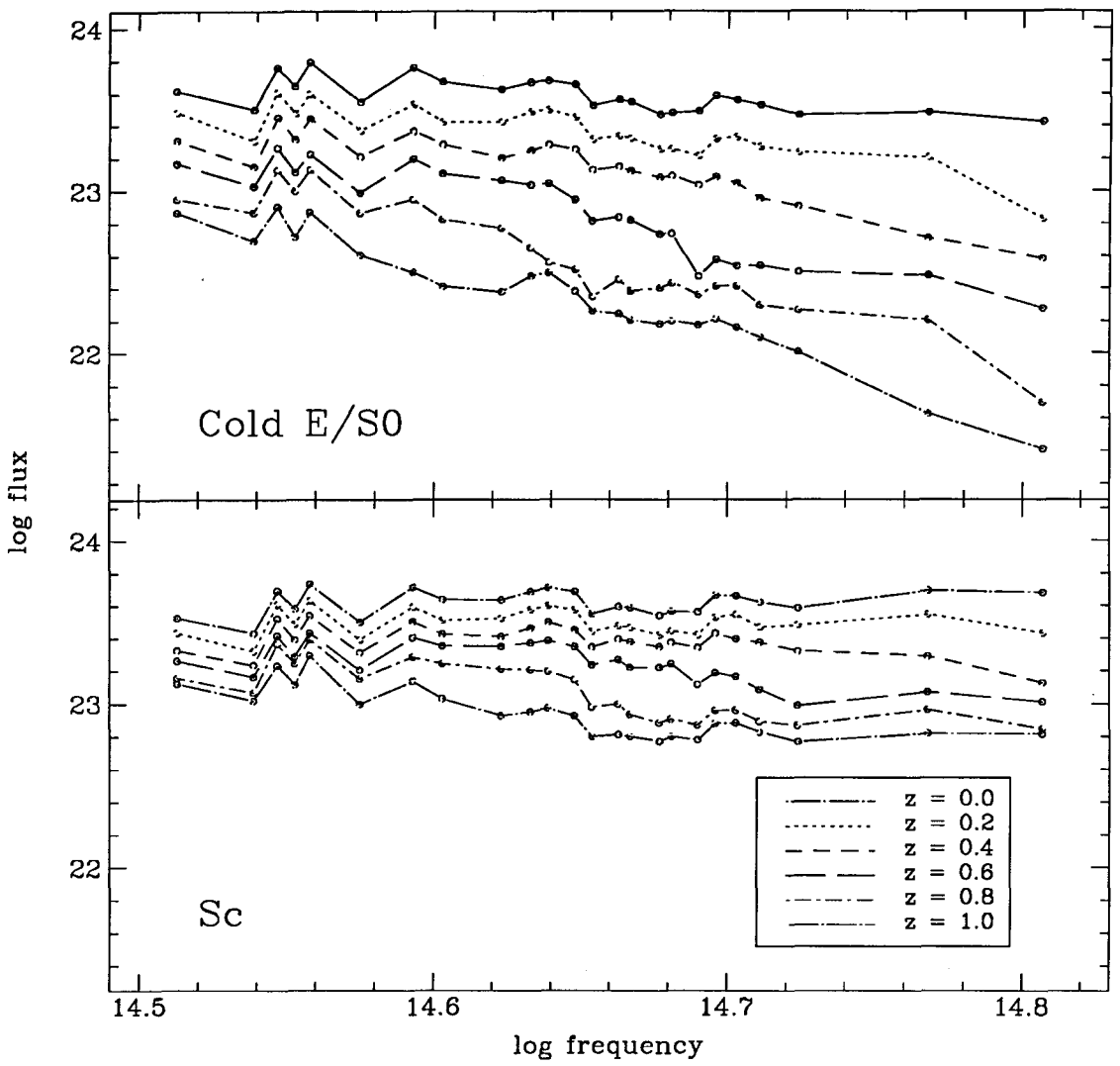

Figure 4.3: The effects of redshift on the spectral energy distributions of an E/S0 and an Sc galaxy. These SEDs are generated by multiplying the redshifted model spectra by the twenty-four filters used to produce the data. Note that the flux units in this figure are $ergs\,s^{-1}cm^{-2}$ rather than $ergs\,s^{-1}cm^{-2}\AA^{-1}$. This figure depicts the templates as they are compared with the data in the fitting program, and the "flux" is a measure of the total light through each filter.

4.4 The Test Sample

In order to test the accuracy of the fitting program, a test sample of spectral energy distributions was identified, consisting of galaxies in the field for which Ellingson, Green, and Yee (1991; hereafter EGY) have measured and published redshifts from multislit spectroscopic data. EGY give redshifts for galaxies in the fields of sixteen quasars, and Yee (pers. comm.) believes about 85 to 90% of the published redshifts are correct. Twelve of the galaxies EGY looked at in the vicinity of 3C281 correspond to the positions of objects identified in the data for this study.

Because two observations of the field were made in each filter, there exist two separate SEDs for each object. A fit was made to each of these, so the consistency of the fit could be studied in the presence of uncertainty in the photometry.

The best-fit redshifts and types assigned to the EGY objects are listed in table 4.2, together with the published redshifts. Both SEDs for object 95 are best fit by a star template (of type 73, M4V). Figure 4.4 shows both spectral energy distributions for these twelve objects, with their best-fit galaxy models overplotted.

There are seven objects in the first list of SEDs for which the difference between the derived and the published redshifts is less than about 0.1, and there are five such objects in the second list. A discussion of the accuracy of the technique based on these results is given in section 6.2.

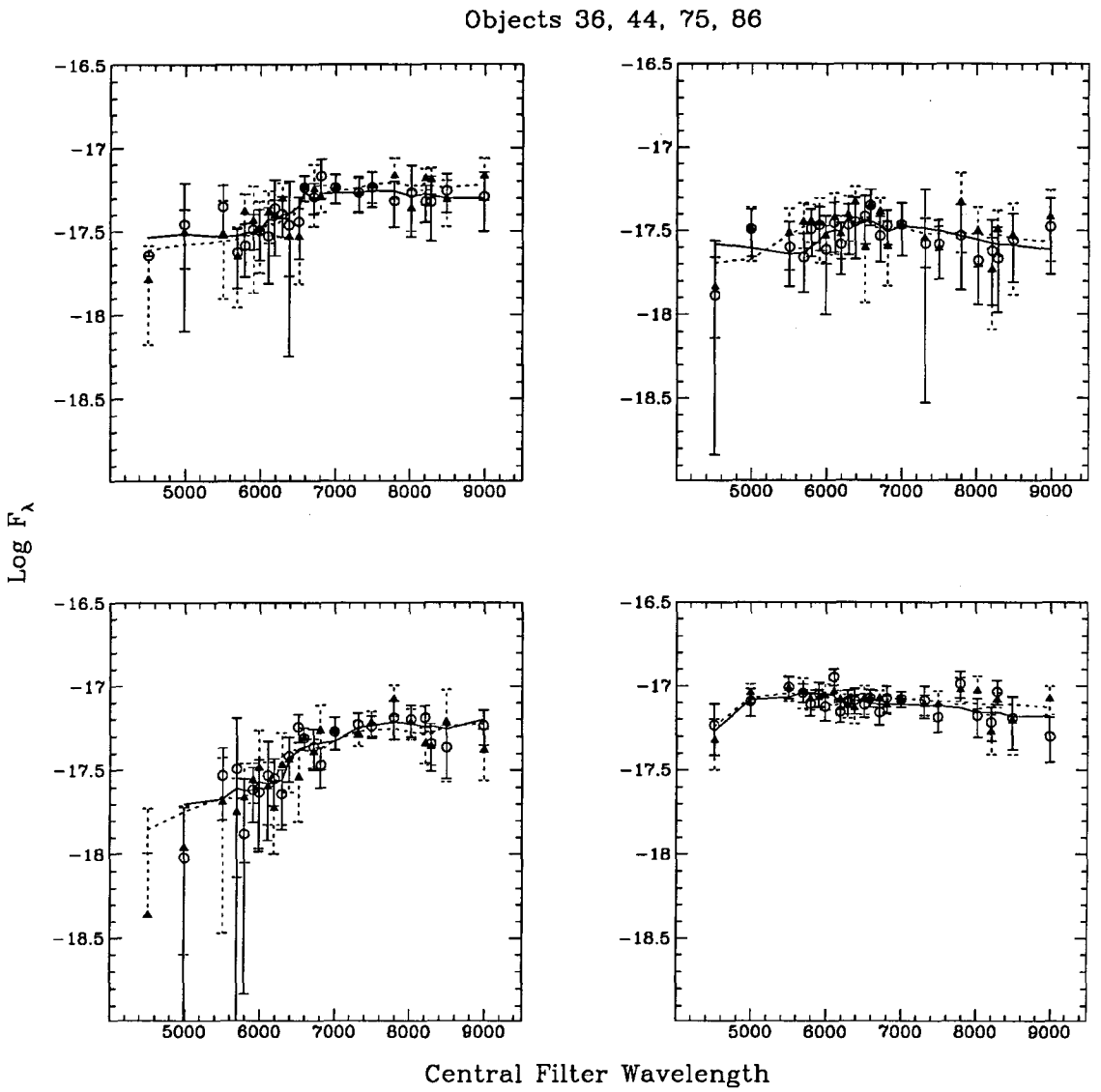

Figure 4.4: Spectral energy distributions for the galaxies from Ellingson, Green, and Yee (1991). The flux units are $ergs\,s^{-1}cm^{-2}\AA^{-1}$. Filled triangles with dotted-line error bars represent the SED produced from the first observation in each filter, hollow circles and solid-line error bars the second SED. The dashed line represents the best-fit galaxy template for the first SED, and the solid line is the best-fit galaxy for the second SED.

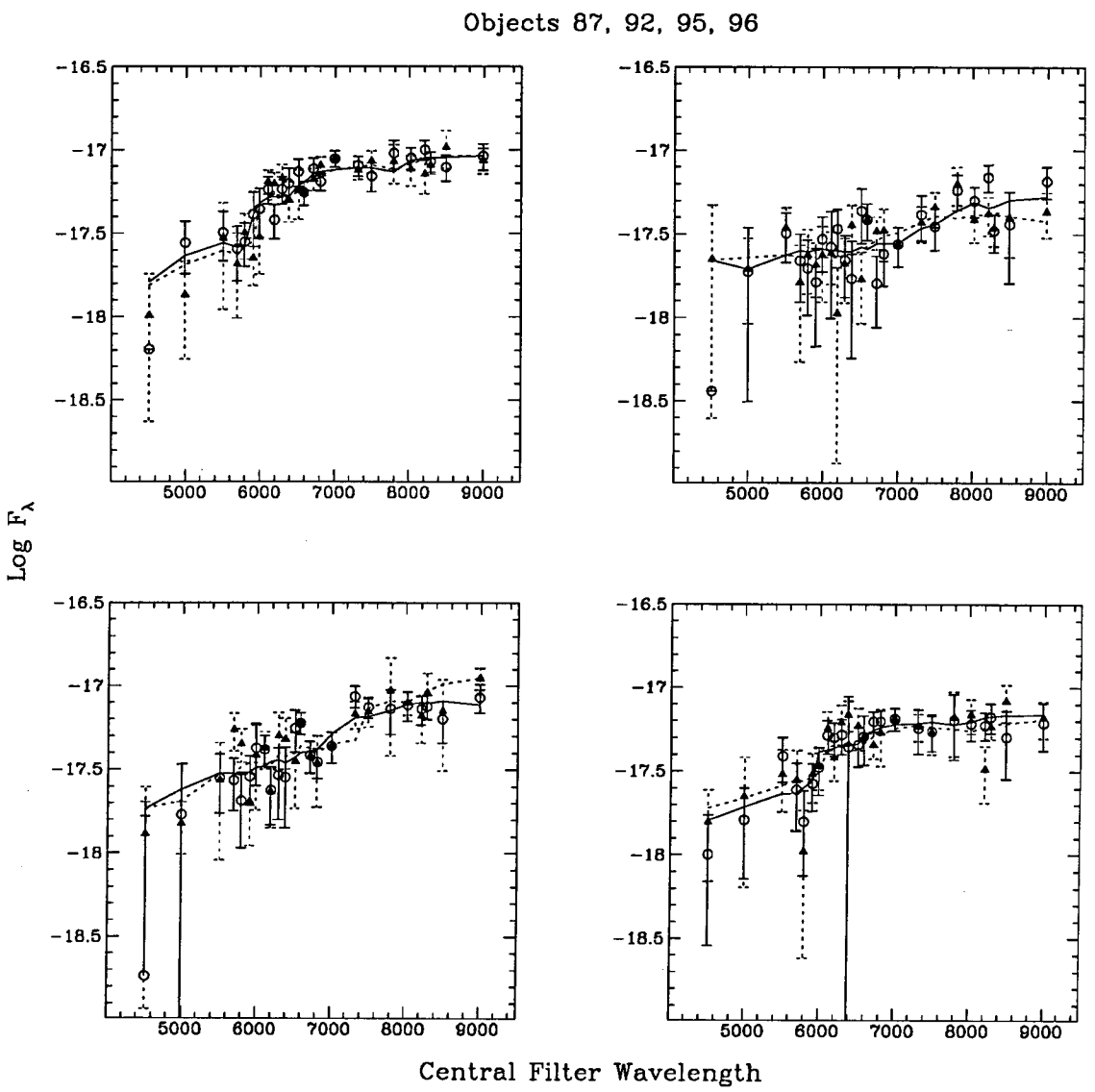
Objects 87, 92, 95, 96
Log F_λ
-16.5
-17
-17.5
-18
-18.5
5000
6000
7000
8000
9000
Central Filter Wavelength

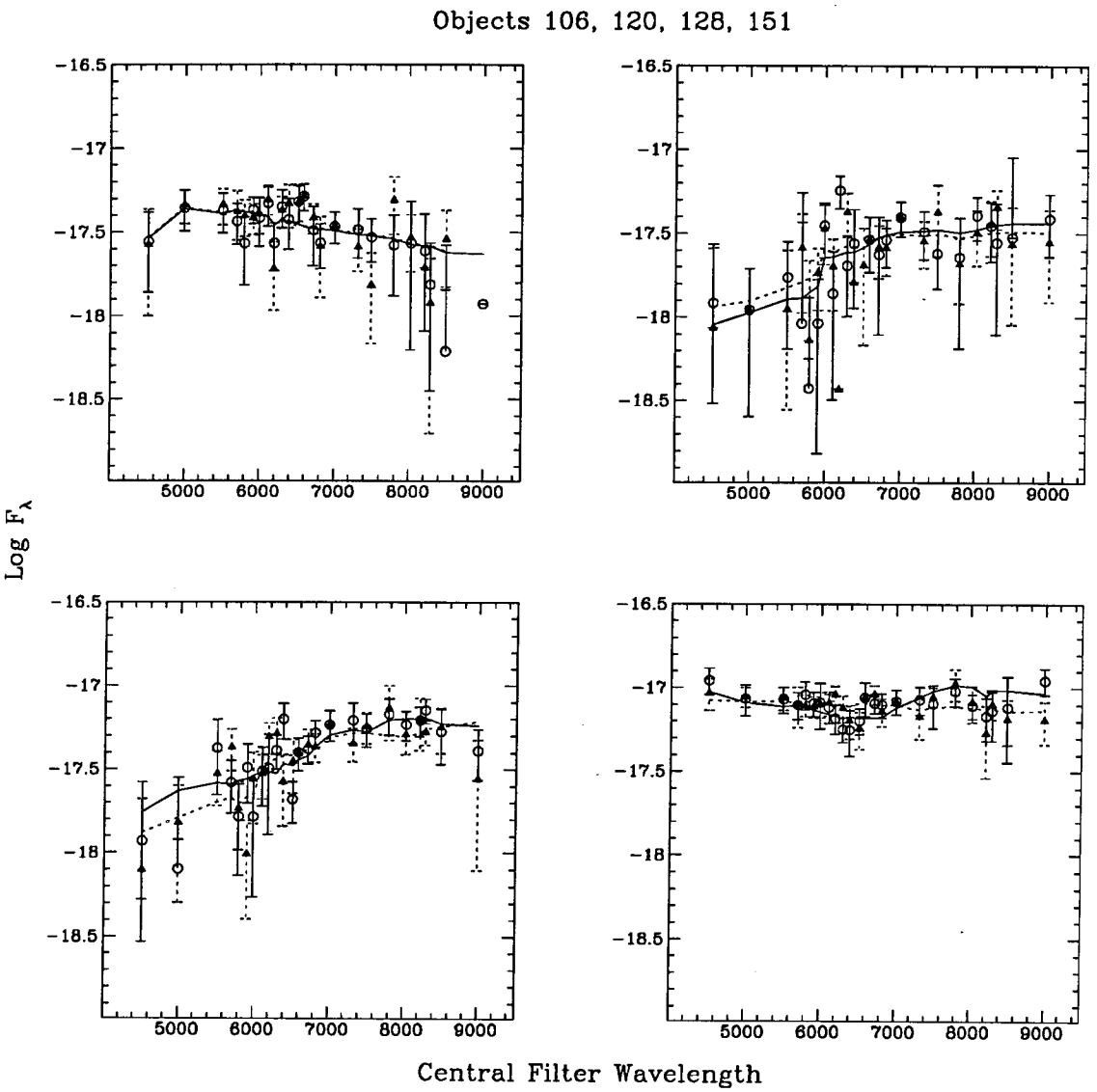
Objects 106, 120, 128, 151
Log F_λ
Central Filter Wavelength
-16.5
-17
-17.5
-18
-18.5
5000
6000
7000
8000
9000

Table 4.2: EGY's published redshifts for objects in the field, and the derived redshifts and galaxy types for both SEDs are listed here. Notice that object 95 is best fit by a stellar model, and one SED for object 92 is also identified as a star. ΔZ_1 and ΔZ_2 are the differences between published and derived redshifts. The R magnitude and median signal-to-noise ratio is shown for each galaxy.

ID	Z_{EGY}	Z_{SED1}	Gal_1		Z_{SED2}	Gal_2		ΔZ_1	ΔZ_2	m_R	S/N
36	0.6090	0.718	3.1	G	0.718	3.9	G	0.109	0.109	21.65	3.4
44	0.46	0.462	4.5	G	0.641	6.0	G	0.002	0.181	22.02	2.7
75	0.6067	0.641	1.4	G	0.679	1.5	G	0.034	0.072	21.65	2.6
86	0.5668	0.245	3.5	G	0.318	4.5	G	-0.322	-0.249	20.90	5.8
87	0.5037	0.567	0.2	G	0.549	0.3	G	0.063	0.045	21.10	4.4
92	0.6053	0.862	4.2	G	0.995	3.4	S	0.257	0.390	22.19	3.0
95	0.4349	0.950	1.3	S	0.841	1.9	S	0.514	0.406	21.67	3.1
96	0.5024	0.603	1.8	G	0.567	1.2	G	0.101	0.065	21.44	3.6
106	0.3266	0.318	6.0	G	0.318	6.0	G	-0.009	-0.009	21.72	3.7
120	0.6025	0.567	2.2	G	0.567	1.3	G	-0.036	-0.036	22.35	2.5
128	0.5513	0.603	1.2	G	0.799	2.7	G	0.052	0.248	21.64	3.3
151	0.5951	0.035	3.2	G	0.972	6.0	G	-0.560	0.370	20.99	5.3

4.5 Systematic Photometry Errors

When the first set of spectral energy distributions and best fits for the EGY test sample was plotted, it appeared that the data points corresponding to certain filters were consistently lower or higher than the best-fit model values. This was confirmed when, for each filter, the mean value of $\frac{flux-best\,model}{model}$ was calculated.

It was clear that the 6200-Å data were significantly lower than the best-fit model in almost every data set. Multiplying the flux level in this filter by a factor of 1.4 tended to bring the point closer to the best-fit model and improve the fit.

It is possible to justify such an alteration to the data because the 6200Å observations were made on the second night, meaning there may have been some extinction from cirrus clouds. No other filters from that night show such a dramatic difference from the models; in fact, some data from that night even produce mean residuals higher than the model flux level.

A high mean residual may indicate a problem with the calibration. In particular, the zero point may have an error ascribable to the nature of the standard star spectrum. The Oke and Gunn spectral energy distribution for the standard star is smoothed, averaging over emission or narrow absorption lines. However, the filters used for these observations are so narrow that, say, an emission line falling in the middle of the filter can affect the calibration perceptibly.

The success of the 6200Å correction in improving the fit was such that similar corrections were made in every filter. Using the set of EGY galaxies with derived redshifts within 0.1 of the published values, an average residual between the observed and model flux was calculated at each filter. The values of these mean residuals were used to apply a multiplicative correction to each of the flux values in the data sets (effectively bringing

the average residual between the "corrected" data and the original best-fit models to zero for the subsample of EGY galaxies).

Best-fit models were assigned to all the "corrected" SEDs. The mean residuals in each filter were then calculated using the entire list of detected objects. If the "correction" of the data made up for real calibration errors or real extinction in the observations, one would expect the mean residuals between this data set and its best-fit models to be significantly smaller than the residuals from the unaltered data set. In fact, the average of the twenty-four mean residuals was very slightly higher for the "corrected" SEDs than for those in which only the value of the 6200Å point was changed.

The attempt to take into account an unknown amount of extinction in the flux values from some filters was therefore unsuccessful. The SEDs from which the redshifts and types were finally derived were chosen to be those in which only the 6200Å flux was adjusted.

4.6 Results

The final list of best fits to the SEDs is shown in table 4.3. The table contains the average redshift, galaxy type, and star type of the fits made to the two SEDs, as well as the difference between the two derived values (indicated by Δ), and a key to whether the best-fit model for each SED is a galaxy or a star. It also lists the χ^2 values for the best star and galaxy fits for both SEDs. As previously discussed, the errors are different in the two data sets and therefore the χ^2 values are not really comparable even between the two SEDs for the same object.

Table 4.4 contains further data which could not be fit into table 4.3 : the position in terms of a distance from the QSO position in arcseconds of right ascension and declination, the simulated R magnitude (the derivation of which is discussed in chapter 5, and some information on the signal-to-noise: the median value of $\frac{f}{\sigma_f}$, the maximum, and the number

Table 4.3: Identifications for the objects in the field. The identifications were made using two separate SEDs for each object. The second column summarizes the classification made for each SED: a "G" indicates that the best fit was to a galaxy template, while "S" stands for a star. The average best-fit redshift, galaxy type, and star type for each object are listed here, together with the difference (Δ) between the two derived values. The χ^2 values for both best-fit galaxy and star templates are in the last four columns. Further information on the objects is in the table following this one.

ID		Z	ΔZ	Gal	ΔGal	Star	ΔStar	χ^2_{gal1}	χ^2_{gal2}	χ^2_{star1}	χ^2_{star2}
1	S G	0.023	0.023	3.2	5.7	33.0	58.0	4.455	0.452	3.485	0.521
2	G G	0.274	0.000	0.9	0.5	64.0	0.0	7.367	5.353	13.723	12.107
3	S S	0.718	0.000	0.0	0.0	74.5	5.0	0.752	1.341	0.620	0.995
4	S S	0.873	0.022	0.0	0.0	80.0	0.0	14.068	16.317	2.940	3.270
5	G G	0.445	0.000	3.6	3.5	62.0	4.0	0.356	0.203	0.399	0.268
6	G G	0.427	0.279	1.7	3.4	65.5	3.0	0.470	0.281	0.589	0.327
7	G G	0.173	0.202	1.5	0.7	62.0	0.0	0.910	1.038	1.491	1.729
8	S G	0.167	0.334	4.8	2.3	46.0	34.0	0.640	0.290	0.633	0.312
9	G G	0.282	0.104	2.2	0.3	62.0	0.0	0.277	0.779	0.333	1.014
10	G G	0.238	0.015	3.7	0.0	53.0	0.0	0.880	1.039	1.270	1.241
11	S G	0.504	0.891	5.8	0.5	61.0	12.0	0.525	0.285	0.520	0.433
12	S S	0.678	0.327	0.0	0.0	75.5	1.0	1.375	0.622	0.939	0.294
13	G G	0.755	0.481	0.7	1.4	70.5	13.0	1.746	0.496	2.674	0.731
14	G G	0.134	0.222	0.6	1.2	63.0	2.0	0.547	0.558	0.612	0.664
15	S S	0.841	0.000	1.1	0.2	71.5	3.0	4.366	4.441	2.363	2.078
16	G G	0.245	0.086	1.1	1.9	63.0	2.0	0.429	0.318	0.537	0.374
17	G S	0.632	0.057	2.5	5.1	66.0	18.0	0.507	1.770	0.570	1.436
18	G G	0.883	0.043	3.7	1.3	68.0	2.0	0.435	0.395	0.511	0.492
19	S G	0.479	0.069	0.0	0.0	73.5	9.0	3.067	0.360	2.556	0.427
20	G G	0.259	0.029	1.7	0.0	62.0	0.0	0.379	1.020	0.699	1.558
21	G G	0.523	0.017	0.6	1.1	68.0	2.0	0.367	1.049	0.697	1.325
22	G G	0.738	0.000	1.9	0.0	69.0	0.0	3.249	1.338	4.415	3.150
23	G G	0.513	0.035	1.0	0.5	68.0	2.0	0.677	0.566	0.824	1.141
24	G G	0.357	0.046	3.8	1.0	60.0	6.0	0.275	0.215	0.306	0.242
25	G G	0.799	0.042	3.8	0.2	67.0	0.0	0.610	0.500	0.688	0.579
26	G G	0.763	0.464	1.1	2.3	70.5	3.0	0.383	0.360	0.685	0.493
27	G G	0.471	0.085	2.8	5.3	66.5	1.0	1.013	0.407	1.060	0.555
28	G G	0.343	0.139	1.9	1.7	64.0	0.0	0.539	0.555	0.653	0.705
29	G S	0.867	0.257	3.0	6.0	69.0	14.0	0.330	2.481	0.412	2.123
30	G S	0.417	0.563	0.6	1.3	66.0	18.0	0.263	1.178	0.296	1.086
31	G G	0.274	0.000	1.3	0.2	63.0	2.0	2.283	2.264	3.721	4.569
32	G G	0.274	0.000	2.1	0.7	62.0	0.0	0.248	0.754	0.321	0.998
33	G G	0.448	0.703	3.4	4.6	63.0	2.0	0.230	0.394	0.274	0.509
34	S S	0.841	0.000	0.9	0.1	75.0	4.0	2.430	1.464	1.325	0.917

ID		Z	ΔZ	Gal	ΔGal	Star	ΔStar	χ^2_{gal1}	χ^2_{gal2}	χ^2_{star1}	χ^2_{star2}
35	G G	0.304	0.490	0.0	0.0	66.0	8.0	0.620	0.502	0.800	0.567
36	G G	0.718	0.000	3.5	0.8	67.0	0.0	0.352	0.172	0.463	0.459
37	G G	0.906	0.131	3.0	6.0	53.5	39.0	0.334	12.644	0.408	12.849
38	G G	0.135	0.000	5.8	0.4	41.0	8.0	8.658	12.281	9.613	13.975
39	S G	0.067	0.110	0.4	0.8	62.0	0.0	0.465	0.627	0.448	0.929
40	G G	0.950	0.090	5.4	1.1	51.0	34.0	0.471	0.306	0.560	0.350
41	S G	0.412	0.065	3.7	4.6	58.5	19.0	0.447	0.327	0.415	0.371
42	G G	0.623	0.149	3.7	3.7	67.5	1.0	0.676	0.832	0.708	1.091
43	G G	0.298	0.135	2.0	1.1	62.0	0.0	1.180	1.894	1.366	2.390
44	G G	0.551	0.179	5.2	1.5	60.0	0.0	0.347	0.228	0.379	0.247
45	G G	0.908	0.175	0.1	0.2	70.0	0.0	0.424	0.518	0.720	0.707
46	G G	0.650	0.095	1.8	1.1	69.0	4.0	0.252	0.363	0.391	0.549
47	G G	0.711	0.217	6.0	0.0	65.0	2.0	1.385	0.625	1.611	0.864
48	G G	0.641	0.000	5.2	0.4	60.5	7.0	0.714	4.480	1.075	5.030
49	G G	0.424	0.213	3.1	2.0	59.5	5.0	0.380	0.532	0.382	0.677
50	G S	0.824	0.252	0.0	0.0	73.0	4.0	5.461	4.283	5.572	4.232
51	G G	0.708	0.020	2.5	2.1	69.0	4.0	0.570	0.342	0.598	0.396
52	G G	0.516	0.174	0.5	1.0	69.0	0.0	0.377	0.203	0.509	0.214
53	G G	0.287	0.383	3.0	5.9	52.5	25.0	3.603	0.234	3.795	0.262
54	S G	0.506	0.844	5.8	0.3	48.0	32.0	0.815	0.413	0.785	0.483
55	S G	0.336	0.648	4.1	3.9	37.5	67.0	3.900	0.248	3.712	0.320
56	G G	0.304	0.060	3.5	0.8	61.0	10.0	0.312	0.509	0.352	0.585
57	S S	0.104	0.089	5.9	0.1	43.5	3.0	2.957	2.561	2.783	2.533
58	G G	0.604	0.074	2.2	0.5	67.5	1.0	0.712	0.786	1.538	1.372
59	S G	0.132	0.169	3.8	4.3	32.0	60.0	1.205	0.261	1.026	0.296
60	G G	0.669	0.057	2.7	1.5	67.0	0.0	0.367	0.475	0.442	0.609
61	G G	0.634	0.632	6.0	0.0	31.5	9.0	0.571	2.080	0.661	2.098
62	G G	0.709	0.098	5.3	0.7	60.5	7.0	0.425	0.453	0.576	0.591
63	G G	0.622	0.038	2.7	1.4	67.5	7.0	0.411	0.792	0.488	0.869
64	G G	0.589	0.219	0.3	0.7	71.5	1.0	0.615	0.398	0.683	0.811
65	G G	0.536	0.247	2.2	1.9	66.5	3.0	0.291	0.521	0.332	0.582
66	G G	0.505	0.018	3.8	4.1	67.0	2.0	1.116	0.123	1.189	0.132
67	G S	0.972	0.045	0.9	1.8	75.0	8.0	0.746	1.003	0.776	0.847
68	G G	0.282	0.294	4.2	3.4	57.5	7.0	0.244	0.726	0.331	0.998
69	S S	0.098	0.126	6.0	0.0	36.5	9.0	0.578	0.361	0.554	0.360
70	G G	0.773	0.264	5.2	1.6	68.0	0.0	0.317	0.567	0.322	0.629
71	S G	0.299	0.573	6.0	0.0	23.0	38.0	5.379	0.858	4.492	0.870
72	S G	0.388	0.286	3.2	2.9	59.5	5.0	0.437	2.396	0.436	2.782
73	G S	0.126	0.207	6.0	0.0	28.0	20.0	0.276	0.776	0.288	0.652
74	G G	0.558	0.054	5.5	0.6	61.5	9.0	0.191	2.059	0.284	2.495

ID		Z	ΔZ	Gal	ΔGal	Star	ΔStar	χ^2_{gal1}	χ^2_{gal2}	χ^2_{star1}	χ^2_{star2}
75	G G	0.660	0.038	1.5	0.1	71.0	0.0	0.450	0.398	0.696	0.468
76	S G	0.775	0.306	1.9	3.8	73.5	5.0	2.280	0.345	1.941	0.355
77	G G	0.524	0.158	0.8	1.6	70.0	2.0	1.235	0.372	1.296	0.453
78	G G	0.711	0.217	1.2	2.5	72.0	2.0	0.746	0.702	1.132	0.862
79	S S	0.283	0.567	5.9	0.1	55.0	0.0	2.185	2.926	1.876	2.751
80	S S	0.018	0.011	6.0	0.0	33.5	3.0	1.739	3.135	1.638	2.934
81	G G	0.728	0.060	2.8	1.9	69.0	4.0	0.513	0.622	0.602	0.763
82	G G	0.650	0.019	3.8	4.3	64.0	14.0	0.489	0.382	0.529	0.430
83	G S	0.576	0.325	0.2	0.4	72.0	8.0	0.215	2.312	0.235	2.271
84	G S	0.492	0.960	6.0	0.0	52.5	31.0	0.250	0.491	0.327	0.413
85	G S	0.275	0.147	6.0	0.0	39.0	6.0	0.310	0.513	0.314	0.510
86	G G	0.281	0.073	4.0	1.0	57.0	2.0	0.320	0.704	0.614	0.831
87	G G	0.558	0.018	0.2	0.1	69.0	0.0	0.593	0.517	1.817	1.071
88	G G	0.497	0.069	2.7	1.2	63.5	3.0	0.425	0.789	0.576	1.117
89	G G	0.961	0.067	0.1	0.2	74.5	9.0	0.579	1.068	0.866	2.744
90	S G	0.799	0.392	0.0	0.0	69.5	13.0	3.210	0.787	2.944	0.985
91	G G	0.672	0.646	1.9	2.6	67.5	1.0	0.415	0.423	0.447	0.512
92	G S	0.928	0.133	3.8	0.8	69.0	4.0	0.452	0.737	0.538	0.727
93	G S	0.030	0.059	6.0	0.0	38.5	7.0	0.742	1.015	0.756	1.001
94	S S	0.047	0.000	6.0	0.0	19.0	4.0	44.314	36.643	16.509	19.331
95	S S	0.896	0.109	1.6	0.6	73.0	0.0	0.817	0.769	0.655	0.569
96	G G	0.585	0.036	1.5	0.6	67.0	0.0	0.716	0.366	1.222	1.098
97	G G	0.578	0.834	4.2	3.6	54.0	0.0	0.381	0.170	0.421	0.226
98	G G	0.928	0.133	3.9	4.0	68.5	7.0	0.857	2.874	1.183	3.726
99	G S	0.012	0.023	4.1	3.8	30.0	56.0	0.253	1.596	0.265	1.382
100	G G	0.514	0.000	0.3	0.6	71.5	1.0	0.724	0.155	0.945	0.248
101	S S	0.054	0.061	6.0	0.0	24.5	15.0	0.457	0.762	0.401	0.641
102	S S	0.067	0.110	6.0	0.0	25.5	17.0	0.523	0.878	0.487	0.760
103	G G	0.527	0.228	3.5	1.7	64.5	1.0	0.903	0.640	0.957	0.681
104	S S	0.650	0.019	0.0	0.0	71.0	2.0	0.554	0.571	0.534	0.452
105	G G	0.737	0.516	4.8	2.5	59.5	11.0	0.424	0.410	0.449	0.502
106	G G	0.318	0.000	6.0	0.0	53.5	3.0	0.796	0.438	0.835	0.467
107	G G	0.245	0.029	4.6	1.1	55.5	7.0	0.925	0.844	1.128	1.019
108	G G	0.350	0.582	3.9	0.9	58.0	12.0	0.898	0.424	0.960	0.459
109	G G	0.780	0.164	3.7	4.5	67.5	7.0	0.073	0.415	0.106	0.475
110	S G	0.252	0.044	4.2	0.8	53.5	1.0	4.651	5.488	3.792	6.682
111	G G	0.691	0.175	0.9	1.9	71.5	1.0	0.242	0.208	0.429	0.338
112	G S	0.385	0.474	0.0	0.0	72.0	14.0	1.862	1.768	1.969	1.527
113	S S	0.875	0.151	3.5	0.1	69.5	3.0	0.656	0.695	0.650	0.604
114	G G	0.540	0.018	3.6	0.2	57.0	0.0	0.884	0.906	0.997	1.268

ID		Z	ΔZ	Gal	ΔGal	Star	ΔStar	χ^2_{gal1}	χ^2_{gal2}	χ^2_{star1}	χ^2_{star2}
115	G G	0.531	0.035	3.0	6.0	60.5	37.0	1.776	3.788	1.951	3.903
116	G G	0.429	0.032	5.4	1.1	57.5	7.0	0.445	1.049	0.498	1.171
117	G S	0.758	0.040	0.6	1.3	73.5	3.0	0.289	2.810	0.321	2.705
118	G G	0.972	0.045	1.6	3.2	34.5	69.0	0.639	1.642	0.825	1.912
119	S G	0.189	0.082	6.0	0.0	46.5	3.0	4.031	5.937	2.920	6.185
120	G G	0.567	0.000	1.8	0.9	67.0	0.0	0.316	0.600	0.389	0.863
121	G G	0.809	0.021	0.2	0.1	70.0	0.0	0.174	0.609	0.434	0.979
122	G G	0.591	0.293	6.0	0.0	60.0	8.0	0.355	3.436	0.454	3.544
123	S S	0.841	0.000	1.9	0.2	71.0	0.0	18.359	18.142	5.966	9.188
124	G G	0.405	0.049	4.7	2.7	56.5	11.0	0.471	1.756	0.635	2.578
125	S G	0.153	0.212	5.4	1.1	37.5	7.0	0.653	0.245	0.645	0.262
126	S S	0.660	0.000	1.8	0.3	71.0	0.0	1.740	1.598	1.220	0.799
127	G G	0.790	0.410	3.0	6.0	71.5	11.0	0.546	0.331	0.737	0.337
128	G G	0.701	0.196	2.0	1.5	70.0	2.0	0.763	0.758	1.155	1.152
129	G S	0.203	0.055	5.6	0.9	48.5	7.0	0.236	0.662	0.308	0.640
130	G S	0.800	0.124	3.0	6.0	72.5	7.0	1.154	5.520	1.351	3.716
131	G G	0.702	0.235	4.8	2.3	66.5	1.0	0.414	1.139	0.460	1.197
132	G S	0.785	0.287	2.5	5.0	70.5	11.0	0.589	3.174	0.617	2.438
133	G G	0.679	0.077	1.0	0.6	70.0	2.0	0.375	0.565	0.494	0.655
134	G G	0.906	0.088	4.6	2.5	68.5	1.0	0.361	0.420	0.568	0.612
135	G G	0.603	0.000	2.8	0.7	65.5	3.0	0.731	0.363	1.001	0.468
136	G G	0.672	0.646	5.8	0.4	49.5	15.0	1.084	0.366	1.109	0.400
137	G G	0.728	0.060	6.0	0.0	62.0	4.0	0.256	0.253	0.355	0.326
138	G G	0.303	0.000	4.0	2.4	56.0	12.0	0.149	0.439	0.201	0.491
139	G G	0.732	0.259	6.0	0.0	50.5	17.0	0.492	11.389	0.574	11.537
140	G G	0.820	0.084	5.5	1.0	53.0	32.0	0.830	3.916	0.896	4.280
141	G G	0.484	0.508	1.0	2.1	64.5	15.0	0.289	0.137	0.369	0.160
142	G G	0.153	0.212	5.2	1.6	41.5	5.0	1.315	1.520	1.434	1.701
143	S S	0.906	0.044	0.9	1.8	75.5	9.0	3.001	0.113	2.958	0.107
144	G G	0.837	0.316	3.0	6.0	59.0	20.0	0.983	0.691	1.302	0.735
145	G G	0.672	0.646	3.0	6.0	52.5	33.0	0.563	0.936	0.622	1.030
146	G S	0.291	0.178	5.3	1.3	54.5	1.0	0.515	0.596	0.588	0.583
147	S S	0.503	0.276	0.2	0.5	71.0	0.0	0.433	0.403	0.402	0.352
148	G S	0.605	0.111	0.1	0.1	71.0	8.0	0.376	0.726	0.529	0.620
149	G S	0.157	0.291	5.1	1.8	33.5	53.0	0.284	1.190	0.311	0.920
150	G G	0.650	0.057	3.8	4.3	66.5	1.0	0.565	0.424	0.725	0.446
151	G G	0.503	0.937	4.6	2.8	51.0	4.0	0.442	0.632	0.662	1.183
152	S G	0.867	0.257	2.3	4.7	66.5	19.0	2.234	2.028	2.223	2.145
153	G G	0.667	0.306	5.2	1.7	64.5	5.0	0.312	0.242	0.367	0.262
154	G G	0.641	0.000	6.0	0.0	57.0	0.0	2.490	0.455	2.941	0.788

ID		Z	ΔZ	Gal	ΔGal	Star	ΔStar	χ^2_{gal1}	χ^2_{gal2}	χ^2_{star1}	χ^2_{star2}
155	G S	0.457	0.184	5.9	0.1	49.5	1.0	0.476	0.403	0.495	0.398
156	G G	0.467	0.664	1.8	0.2	65.5	7.0	0.627	0.277	0.692	0.320
157	G G	0.748	0.060	4.6	2.9	64.5	1.0	0.305	0.316	0.310	0.371
158	G G	0.632	0.131	0.0	0.0	72.0	0.0	1.599	0.726	1.698	0.875
159	G G	0.535	0.212	5.2	1.7	65.0	0.0	0.337	0.256	0.345	0.274
160	G G	0.065	0.061	5.8	0.1	41.0	0.0	0.582	0.330	0.632	0.349
161	S S	0.529	0.540	1.3	2.6	67.0	0.0	18.138	16.562	11.747	12.411
162	G G	0.698	0.000	0.3	0.6	70.5	3.0	0.520	2.331	0.841	3.036
163	S G	0.739	0.120	0.9	1.7	73.0	4.0	0.912	0.265	0.868	0.307
164	G G	0.831	0.147	3.0	6.0	26.0	0.0	0.782	0.832	0.875	0.869
165	S G	0.585	0.036	0.0	0.0	75.5	7.0	1.385	0.372	1.246	0.408
166	G G	0.140	0.210	4.7	0.8	48.5	7.0	0.608	0.638	0.678	0.654
167	G G	0.176	0.108	4.0	1.0	46.0	0.0	1.668	1.007	1.744	1.178
168	G G	0.467	0.583	6.0	0.0	46.0	18.0	0.300	0.600	0.309	0.637
169	G G	0.326	0.016	5.1	1.7	52.5	7.0	0.523	0.279	0.572	0.303
170	G G	0.516	0.174	5.0	2.0	53.0	22.0	0.487	0.418	0.503	0.486
171	G G	0.811	0.187	3.7	4.7	56.5	31.0	0.503	0.212	0.609	0.317
172	G G	0.625	0.187	6.0	0.0	53.0	8.0	0.502	0.421	0.529	0.490
173	G G	0.533	0.744	5.2	1.6	56.5	23.0	0.275	0.370	0.285	0.462
174	S G	0.972	0.045	4.0	2.2	68.0	2.0	0.570	0.405	0.541	0.513
175	G G	0.365	0.095	0.6	1.3	64.0	0.0	1.175	3.902	2.848	5.400
176	G G	0.084	0.050	4.4	0.7	46.5	1.0	0.322	0.633	0.400	0.654
177	G G	0.281	0.014	1.1	0.0	64.0	0.0	6.781	3.752	9.500	6.536
178	G G	0.887	0.217	0.4	0.6	72.0	0.0	0.634	0.526	0.806	0.546
179	G G	0.567	0.675	0.9	1.9	65.5	7.0	0.341	4.530	0.360	4.565
180	G G	0.738	0.000	0.2	0.5	72.0	0.0	0.160	0.520	0.286	0.919
181	G G	0.238	0.015	5.8	0.5	53.5	3.0	4.424	4.499	4.609	5.973
182	G S	0.730	0.179	0.7	1.4	71.5	5.0	0.216	1.783	0.226	1.668
183	G G	0.577	0.127	3.0	6.0	65.5	17.0	0.744	0.830	0.866	1.005
184	G G	0.877	0.237	4.6	0.8	65.5	3.0	0.575	0.357	0.709	0.448

of filters (out of a possible twenty-four) in which $\frac{f}{\sigma_f} \geq 3.0$.

Forty-two of the objects in the list were classified as galaxies according to one SED and as stars according to the other. Most of these objects were very faint, so the noise in the SEDs probably obscured the spectral shape and did not permit a definite identification. A few, however, are quite bright, notably those numbered 39, 110, and 119, for which all the data points have signal-to-noise above 3.0. Objects 72, 92, and 129 have 12, 12, and 19 points with $S/N \geq 3$ respectively. It is likely that these belong to classes of galaxies not included in the range of models considered in the fitting program; they may be emission-line objects. Objects such as 50, which has a median signal-to-noise in its data set of 1.6, and a maximum of 9.4, with only two points having $S/N \geq 3$, may represent emission-line objects.

Photometric data for the 3C281 field were taken from Yee, Green, and Stockman (1986), and Yee (pers. comm.) provided classifications for these objects (i.e. galaxy or star) based on the shape of each image. Table 4.5 summarizes the type classifications and magnitudes of the thirty-three objects which appear in this data set. One of the objects, number 94, is the QSO itself. Of the remaining thirty-two objects, Yee's analysis indicates that eight are stars and twenty-four are galaxies. The template-fitting program identified five of the objects as a star from one SED and a galaxy from the other. Excluding those five objects, star types have been assigned to 2/6 of Yee's remaining stars, and galaxy types to 20/21 of his galaxies.

The field size for the data presented by Yee, Green, and Stockman was 3.64 square arcminutes, and they listed the limiting R magnitude for the 3C281 field as 23.4. The corresponding limit in V is roughly 24 magnitudes, and the Bahcall-Soneira model (Ratnatunga and Bahcall 1985) predicts between four (for $V_{lim} = 23$) and seven (for $V_{lim} = 25$) stars in the field. This suggests the possibility that one or more of Yee's stars is actually

Table 4.4: The position of each object is given as a distance in arcseconds of right ascension and declination from the position of the QSO. The R magnitude and uncertainty are derived in chapter 5 but listed here for completeness. The three signal-to-noise values represent the median S/N value from all the observations, the maximum value of the S/N, and the number of filters in which the S/N was 3.0 or greater.

ID	ΔRA (")	ΔDec	m_R	σ_{m_R}	Median S/N	Max S/N	No. S/N≥3.0
1	-159.78	20.66	22.54	0.84	2.2	3.7	3
2	-159.09	0.34	17.55	0.04	23.9	31.0	24
3	-158.06	18.25	21.35	0.18	4.5	8.3	17
4	-157.37	-27.55	20.19	0.08	7.6	20.4	23
5	-156.68	8.26	22.79	0.73	1.5	3.9	1
6	-154.27	82.64	21.82	0.26	2.6	4.8	9
7	-153.92	54.06	20.08	0.10	8.4	11.6	24
8	-152.20	-39.26	23.09	1.40	1.1	3.4	2
9	-151.86	-24.45	21.29	0.16	4.1	6.6	17
10	-146.35	19.97	20.38	0.09	6.4	14.3	23
11	-141.53	-27.89	23.14	0.91	1.4	3.1	1
12	-141.53	26.51	23.34	0.00	1.1	2.6	0
13	-139.46	88.15	22.25	0.63	2.3	3.6	3
14	-135.67	-14.12	21.00	0.11	5.2	7.9	22
15	-135.67	-64.05	19.96	0.06	10.7	20.8	24
16	-134.99	2.07	21.93	0.21	2.9	6.9	10
17	-131.20	61.64	23.23	0.74	1.4	2.5	0
18	-130.85	13.77	22.04	0.33	2.5	6.6	8
19	-130.16	26.17	22.50	0.38	1.9	2.8	0
20	-125.69	-11.36	20.21	0.08	8.7	13.2	24
21	-125.69	-51.31	21.93	0.29	3.1	6.1	14
22	-125.00	105.72	20.59	0.13	6.3	11.2	23
23	-121.56	-48.21	21.30	0.18	4.4	7.5	18
24	-118.46	54.41	22.32	0.37	2.2	3.3	6
25	-117.42	80.58	22.16	0.32	3.0	6.0	12
26	-112.95	18.25	22.83	0.64	1.8	3.9	1
27	-109.50	-26.86	22.76	0.71	1.8	5.3	2
28	-108.81	-9.30	20.36	0.07	8.9	14.7	24
29	-107.78	-1.72	23.32	0.60	1.4	3.3	1
30	-105.37	46.14	23.70	0.85	1.2	2.0	0
31	-104.68	-79.89	18.48	0.04	18.6	25.1	24
32	-103.99	40.29	20.80	0.09	5.7	11.0	19
33	-103.99	25.14	22.57	0.48	1.7	2.9	0
34	-102.62	1.03	20.73	0.09	7.7	17.9	20

ID	ΔRA (")	ΔDec	m_R	σ_{m_R}	Median S/N	Max S/N	No. S/N≥3.0
35	-101.58	14.12	23.49	0.00	1.3	2.3	0
36	-96.07	23.76	21.65	0.22	3.4	6.9	13
37	-95.73	49.93	23.43	0.91	1.1	2.1	0
38	-88.50	-91.94	18.86	0.04	19.3	27.9	24
39	-87.46	4.13	20.66	0.08	7.8	12.5	24
40	-83.33	-9.30	23.37	2.50	1.1	2.8	0
41	-81.61	-41.32	22.93	0.00	1.8	4.1	1
42	-77.48	95.04	22.90	0.85	1.6	3.3	1
43	-77.48	-60.61	19.84	0.06	10.7	15.7	24
44	-76.79	-2.07	22.02	0.25	2.7	4.9	9
45	-70.59	15.15	22.78	0.49	2.1	5.7	5
46	-69.90	100.89	22.75	1.48	1.5	4.8	6
47	-64.39	-73.00	22.14	0.38	2.1	6.5	3
48	-62.67	97.80	21.36	0.16	3.9	7.6	19
49	-62.33	6.89	20.57	0.10	7.1	11.3	23
50	-60.26	68.53	23.32	0.00	1.6	9.4	2
51	-59.57	30.99	21.88	0.26	3.2	8.6	13
52	-57.16	37.19	22.84	0.75	1.2	2.3	0
53	-54.06	10.67	22.32	0.32	2.2	12.4	5
54	-48.55	-49.24	22.81	0.57	1.3	2.8	0
55	-48.21	-33.06	22.83	0.61	1.8	3.2	4
56	-47.86	48.21	22.29	0.39	2.2	3.6	3
57	-46.49	29.61	21.12	0.11	4.7	12.2	17
58	-45.11	-14.81	20.92	0.12	5.4	12.3	21
59	-44.77	102.62	23.31	0.77	1.1	1.9	0
60	-44.08	22.04	22.57	0.44	2.1	4.0	3
61	-44.08	-107.09	23.23	2.23	1.2	2.2	0
62	-43.04	88.15	22.28	0.36	2.1	4.1	6
63	-40.63	14.12	22.84	0.51	1.5	3.2	1
64	-39.60	-66.12	21.56	0.22	3.6	8.1	17
65	-35.12	-28.24	22.21	0.36	2.2	4.0	5
66	-33.75	52.00	22.85	0.00	1.3	6.2	1
67	-33.40	12.05	23.51	0.93	1.5	4.0	1
68	-32.71	-49.93	21.03	0.14	4.7	9.0	19
69	-27.89	-95.04	22.50	0.33	1.8	3.7	4
70	-26.17	-21.69	23.09	0.91	1.3	2.2	0
71	-25.48	73.69	22.56	0.53	1.8	7.7	2
72	-25.48	-90.56	21.73	0.23	2.9	5.7	12
73	-24.45	-81.27	23.37	0.89	1.4	2.4	0
74	-23.76	-42.70	21.78	0.24	3.1	5.6	11

ID	ΔRA (")	ΔDec	m_R	σ_{m_R}	Median S/N	Max S/N	No. S/N≥3.0
75	-19.63	48.55	21.65	0.26	2.6	6.5	10
76	-19.28	16.87	23.10	0.46	1.5	2.6	0
77	-18.59	19.97	22.28	0.34	2.4	7.1	9
78	-17.56	-34.09	22.92	0.72	1.7	3.3	2
79	-17.56	-85.74	21.17	0.12	4.4	11.6	20
80	-14.46	50.28	22.83	1.28	1.6	3.3	1
81	-14.12	25.14	22.65	0.55	2.0	3.2	1
82	-13.09	-71.62	23.02	0.61	1.5	3.1	1
83	-12.74	-6.20	22.66	0.44	1.8	3.0	0
84	-11.71	-76.45	22.66	0.52	1.4	3.0	0
85	-9.64	-94.01	23.18	0.71	1.2	3.4	1
86	-8.26	68.87	20.90	0.10	5.8	9.8	22
87	-7.23	14.12	21.10	0.17	4.4	9.0	19
88	-6.89	5.51	21.58	0.20	3.3	5.1	14
89	-6.89	-37.53	22.33	0.34	2.4	7.0	9
90	-5.17	70.94	23.06	0.98	1.5	3.2	1
91	-3.79	-19.63	22.84	0.70	1.7	2.8	0
92	-1.03	-5.17	22.19	0.34	3.0	4.5	12
93	-0.34	3.44	22.45	0.38	2.2	4.2	6
94	0.00	0.00	17.37	0.04	26.9	36.4	24
95	0.69	-98.83	21.67	0.21	3.1	6.6	12
96	2.41	20.32	21.44	0.19	3.6	6.5	15
97	2.75	68.18	23.24	1.06	1.2	2.3	0
98	3.10	-0.34	22.50	0.35	2.7	6.2	10
99	4.48	-56.82	23.24	0.56	1.3	3.0	0
100	5.85	48.21	23.13	0.00	1.3	3.7	1
101	7.58	-17.91	22.64	0.34	2.0	5.6	4
102	7.58	97.45	22.63	0.49	2.2	4.2	1
103	10.33	-52.00	20.83	0.09	6.7	11.2	22
104	12.05	-8.26	22.63	0.55	1.9	5.6	3
105	12.40	-3.44	23.07	0.89	1.3	2.4	0
106	13.43	-22.38	21.72	0.23	3.7	5.5	14
107	13.77	-108.47	21.10	0.14	5.4	8.3	20
108	15.50	-32.02	22.45	0.38	2.1	3.7	4
109	15.84	82.64	23.40	0.61	1.3	2.2	0
110	20.32	-105.37	16.89	0.04	26.7	35.3	24
111	21.35	15.84	22.32	0.33	2.6	4.4	7
112	23.07	72.31	23.00	0.57	1.4	8.2	1
113	23.76	-42.70	22.92	0.64	1.6	4.3	2
114	24.79	86.78	21.44	0.21	3.3	5.8	17

ID	ΔRA (")	ΔDec	m_R	σ_{m_R}	Median S/N	Max S/N	No. S/N≥3.0
115	24.79	-17.56	22.94	0.00	1.6	3.1	1
116	25.14	35.47	21.25	0.14	5.0	8.7	22
117	25.48	-61.29	22.58	0.71	1.6	3.4	2
118	26.51	59.23	22.77	0.72	2.0	4.5	1
119	27.55	33.40	18.22	0.04	24.0	28.9	24
120	27.89	-71.28	22.35	0.34	2.5	4.3	5
121	32.02	-60.61	21.72	0.25	3.3	8.4	13
122	32.71	25.14	23.20	0.00	0.8	2.4	0
123	35.12	-76.45	16.55	0.04	27.2	34.5	24
124	36.16	51.65	20.42	0.11	7.2	10.9	24
125	38.22	17.22	23.30	1.82	1.4	2.9	0
126	39.94	-6.54	20.85	0.11	6.2	11.1	23
127	39.94	-63.70	23.29	1.58	1.0	3.7	1
128	40.29	-11.71	21.64	0.25	3.3	6.0	13
129	42.36	-75.76	21.39	0.15	3.7	5.8	19
130	45.45	66.12	22.91	1.11	1.8	3.4	1
131	47.52	-11.71	22.92	0.65	1.4	3.0	0
132	47.86	-59.23	23.25	0.00	1.2	2.5	0
133	47.86	-61.98	22.52	0.48	1.5	4.2	5
134	50.96	61.64	21.95	0.33	2.8	5.3	10
135	53.03	-44.42	22.34	0.36	2.5	4.0	11
136	53.03	22.38	22.97	0.47	1.2	4.2	1
137	53.37	54.41	23.02	0.60	1.6	2.9	0
138	54.06	99.17	23.00	0.53	1.1	2.6	0
139	54.41	-86.78	23.00	0.80	1.5	3.1	1
140	57.51	87.46	23.25	1.33	1.0	3.6	1
141	77.82	3.44	22.99	1.10	1.1	2.8	0
142	78.51	58.88	21.05	0.13	4.1	8.4	19
143	79.89	26.86	23.95	0.00	0.8	6.6	1
144	81.27	-50.62	23.48	0.00	1.4	5.0	1
145	82.99	22.38	23.28	0.00	1.1	2.2	0
146	83.68	-80.23	22.52	0.39	2.0	4.1	4
147	88.84	-24.10	22.28	0.40	2.5	4.4	6
148	88.84	12.05	23.64	0.00	0.8	2.1	0
149	89.19	-101.58	23.10	0.69	1.0	2.3	0
150	90.91	21.35	22.84	0.66	1.3	3.1	1
151	92.29	-84.71	20.99	0.12	5.3	7.7	23
152	93.32	2.41	22.97	0.47	1.5	2.5	0
153	94.01	-44.42	23.62	0.00	0.9	2.0	0
154	98.48	61.98	20.73	0.11	4.6	13.5	20

ID	ΔRA (")	ΔDec	m_R	σ_{m_R}	Median S/N	Max S/N	No. S/N≥3.0
155	98.48	43.39	22.41	0.33	2.1	3.5	2
156	101.58	-32.71	22.61	0.60	1.8	3.4	1
157	103.31	66.12	22.94	0.70	1.2	3.0	0
158	103.31	-52.34	22.55	0.51	1.8	8.1	3
159	103.65	4.13	22.85	0.52	1.3	2.8	0
160	113.64	67.15	21.66	0.27	3.2	6.1	13
161	116.39	78.17	15.68	0.04	27.5	36.0	24
162	116.39	35.12	22.24	0.65	2.4	6.0	7
163	117.42	-39.26	23.24	0.00	1.3	1.9	0
164	121.56	-70.59	23.35	1.04	1.2	2.6	0
165	123.28	-38.57	22.66	1.58	1.2	3.2	1
166	125.34	-14.12	21.82	0.22	3.3	5.4	14
167	126.03	10.33	20.85	0.12	5.8	8.6	22
168	127.07	-7.92	22.53	0.44	1.6	3.5	1
169	127.75	79.89	22.28	0.42	2.2	3.1	2
170	127.75	-90.56	23.05	0.00	1.3	2.4	0
171	129.13	-44.42	22.61	0.56	1.8	5.1	3
172	133.26	88.84	21.73	0.23	3.2	5.8	13
173	133.26	16.18	22.92	0.53	1.6	2.6	0
174	136.02	-97.45	22.24	0.42	2.1	4.3	7
175	136.02	-102.62	19.44	0.06	12.3	17.5	24
176	138.77	69.21	22.15	0.35	2.5	6.1	7
177	141.18	32.71	18.93	0.05	16.2	22.8	24
178	141.87	-45.80	22.65	0.66	1.7	3.8	3
179	142.91	-101.24	23.01	0.92	1.0	2.7	0
180	143.25	-40.29	21.77	0.33	2.5	5.1	8
181	143.94	-28.24	18.34	0.04	21.5	27.5	24
182	143.94	-92.29	22.72	0.60	1.5	2.7	0
183	146.00	-73.69	22.72	1.48	1.4	2.6	0
184	147.04	45.45	22.32	0.41	2.1	4.2	3

a compact or unresolved galaxy, or bright galactic nucleus, with the appearance of a star.

In all, the list contains 184 objects, of which 122 are classified as galaxies according to both SEDs, and twenty as stars. The QSO 3C281, object 94, is classified as a type B9V star; its best-fit galaxy type is 6.0 at z= 0.047. Its real redshift, from EGY, is 0.602. Of course, the fitting program includes no model spectrum for an unusual object like a QSO, so neither class nor derived redshift was expected to be accurate.

The distributions of best-fit galaxy types and best-fit star types are plotted in the two histograms shown in figure 4.5. The solid-line histogram shows the distribution for the whole sample, while the shaded histogram shows the distribution only for those objects classified by the fitting program as galaxies in the first plot and as stars in the second.

The distribution of identified galaxy types seems approximately uniform when only those objects identified as galaxies in both SEDs are considered. Other objects seem to be preferentially assigned extreme types (0.0 and 6.0) but, as discussed earlier, many of these objects either are too faint to be uniquely fit by a model or are unusual types not represented in the set of galaxy models used by the fitting program.

Recalling that types 0 and 1 represent UV-cold and -hot E/S0 galaxies and 2 through 5 are spirals, the distribution of galaxy types suggests that there are very roughly three times as many spirals as early-type galaxies in the field. The *Revised Shapley-Ames Catalog of Bright Galaxies* (Sandage and Tammann 1987) finds a slightly lower ratio of spirals to E/S0s for relatively local galaxies (the completeness limit of the catalog is $m_{pg} = 13.2$). It is possible that a Butcher-Oemler effect is observed in the cluster at $z \approx 0.6$, increasing the number of blue late-type galaxies in the field.

There are only twenty objects classified as stars according to both SEDs, of which thirteen are of type 64 (K5) or later. This is not unexpected given that the line of sight to the cluster passes through the disk of the Galaxy. The QSO's position in 1950 galactic

Table 4.5: Magnitudes and type classifications for the set of calibration galaxies. R magnitudes, shown in the second column, were taken from Yee, Green, and Stockman (1986) to calibrate the instrumental magnitudes, and the resulting calibrated magnitudes appear in the third column, followed by their uncertainties. Yee's classifications (s=star, g=galaxy) based on the image shape are given in the fifth column, next to the classifications derived from template-fitting. Where the two SEDs classed the object as a star and a galaxy, both are noted. A "y" following indicates that both image shape and SED-fitting methods yield the same classification. The last column contains the median signal-to-noise.

Object	R_{YGS86}	R_{calib}	σ_R	Class (Yee)	Class (SED)	Match?	S/N
49	20.74	20.568	0.100	g	g	y	7.1
51	22.15	21.878	0.264	s	g	n	3.2
52	22.51	22.845	0.749	g	g	y	1.2
53	22.63	22.315	0.318	g	g	y	2.2
55	22.63	22.826	0.607	g	sg	-	1.8
56	22.02	22.293	0.386	s	g	n	2.2
57	20.94	21.116	0.110	g	s	n	4.7
58	20.84	20.917	0.121	g	g	y	5.4
60	22.61	22.569	0.444	s	g	n	2.1
63	22.27	22.839	0.506	g	g	y	1.5
65	22.28	22.208	0.356	g	g	y	2.2
67	23.35	23.511	0.927	s	gs	-	1.5
75	21.72	21.645	0.258	g	g	y	2.6
77	22.04	22.283	0.342	g	g	y	2.4
78	22.49	22.924	0.717	s	g	n	1.7
81	22.05	22.647	0.545	g	g	y	2.0
83	22.56	22.662	0.435	g	gs	-	1.8
87	20.96	21.105	0.166	g	g	y	4.4
88	21.11	21.577	0.205	g	g	y	3.3
89	21.76	22.330	0.340	g	g	y	2.4
91	22.48	22.845	0.698	g	g	y	1.7
92	22.25	22.191	0.339	g	gs	-	3.0
94	17.27	17.374	0.037	qso	s	-	26.9
96	21.58	21.444	0.188	g	g	y	3.6
101	22.38	22.641	0.343	s	s	y	2.0
104	22.21	22.631	0.546	s	s	y	1.9
105	23.01	23.066	0.891	g	g	y	1.3
106	21.60	21.715	0.230	g	g	y	3.7
108	23.16	22.455	0.375	g	g	y	2.1
111	22.06	22.319	0.334	g	g	y	2.6
116	20.98	21.245	0.142	g	g	y	5.0
119	18.38	18.223	0.038	s	sg	-	24.0
128	22.00	21.639	0.248	g	g	y	3.3

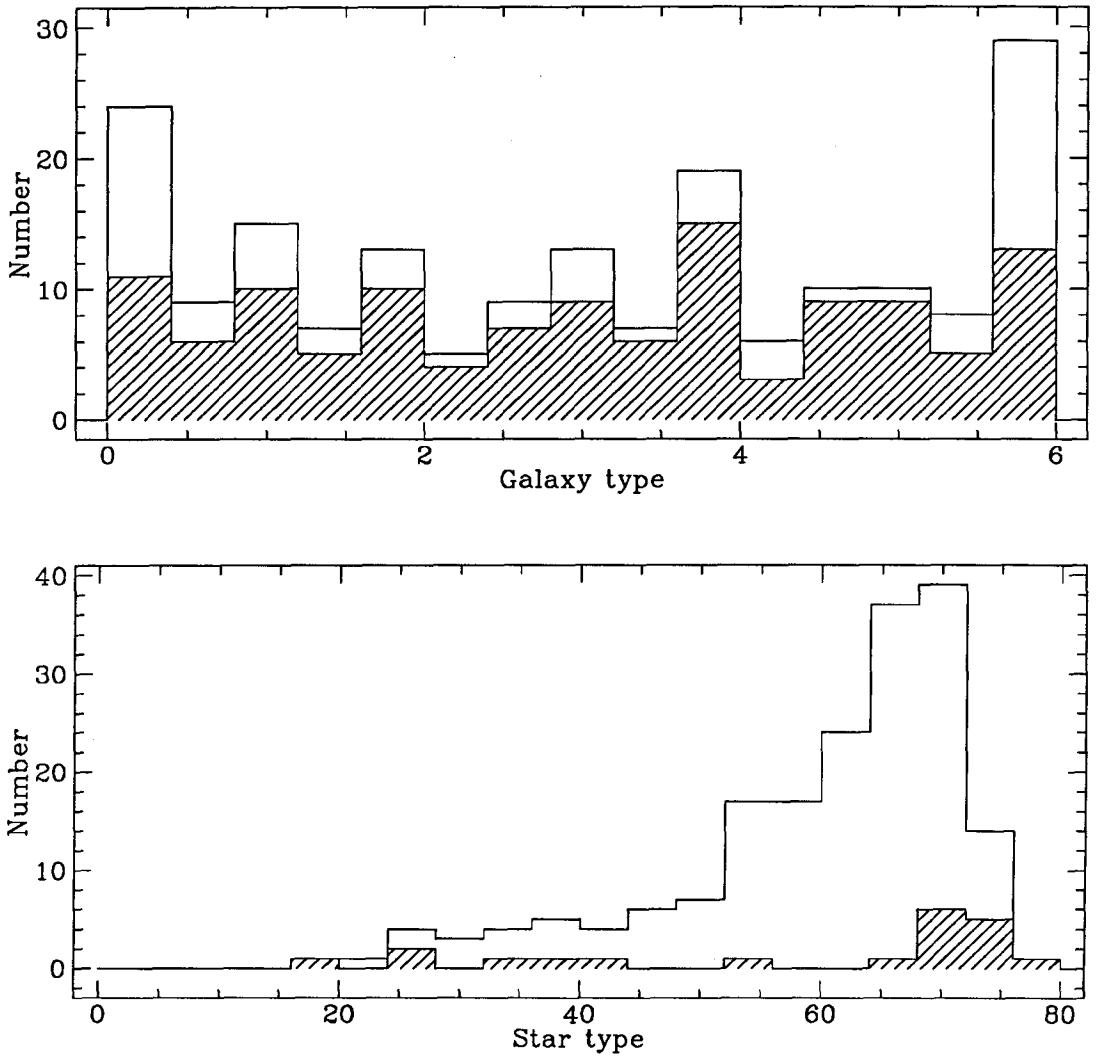

Figure 4.5: The upper histogram is the distribution of average best-fit galaxy types for the entire list of detections. The shaded histogram shows the distribution only for objects classified as galaxies according to both SEDs. The lower histogram shows the distribution of best-fit star types, and the twenty objects in the shaded histogram are those identified as stars from both SEDS.

coordinates is $l = 314.50°, b = 69.20°$. Star counts in the direction of the field may be estimated using the Bahcall-Soneira model (e.g. Ratnatunga and Bahcall 1985). Assuming a limiting R magnitude for these data of about 22.5 (chapter 5), which corresponds over all star types to an approximate limit of V=23, the model predicts that about twenty-one stars will be seen in the field, of which fourteen will be of types K and M. These numbers are close to those observed in the field.

The distribution of assigned redshifts, shown in figure 4.6, is quite interesting. In this figure, objects classified as galaxies according to both SEDs are shown by the shaded histogram. All but two of the objects with best-fit galaxy redshifts of 0.1 or below are classed as stars. One would expect the number of galaxies to increase with redshift, since at greater distances a larger volume is being sampled per redshift bin. At high redshifts, however, the faintest objects will not be seen, so only the most luminous will be sampled, and the volume density of detected galaxies will decrease with redshift (ignoring evolution).

These biasing effects are almost impossible to correct with these data, since there are large uncertainties in both redshift and magnitude. This distribution therefore does not represent a luminosity function for the field. It is interesting to notice, however, that there seems to be an enhancement in the number of galaxies near the quasar redshift, where one might expect to find cluster galaxies. Table 4.6 lists the fifty-eight objects with redshifts within 0.1 of the quasar redshift 0.602. However, the "enhancement" in the redshift distribution may only represent the natural peak created by the combination of the two biases, one causing a dropoff in counts at high redshift and the other causing a dropoff at low redshift.

The type identifications and redshifts should be more accurate for objects of higher signal-to-noise ratio. Figure 4.7 shows the redshift distribution from figure 4.6, but in-

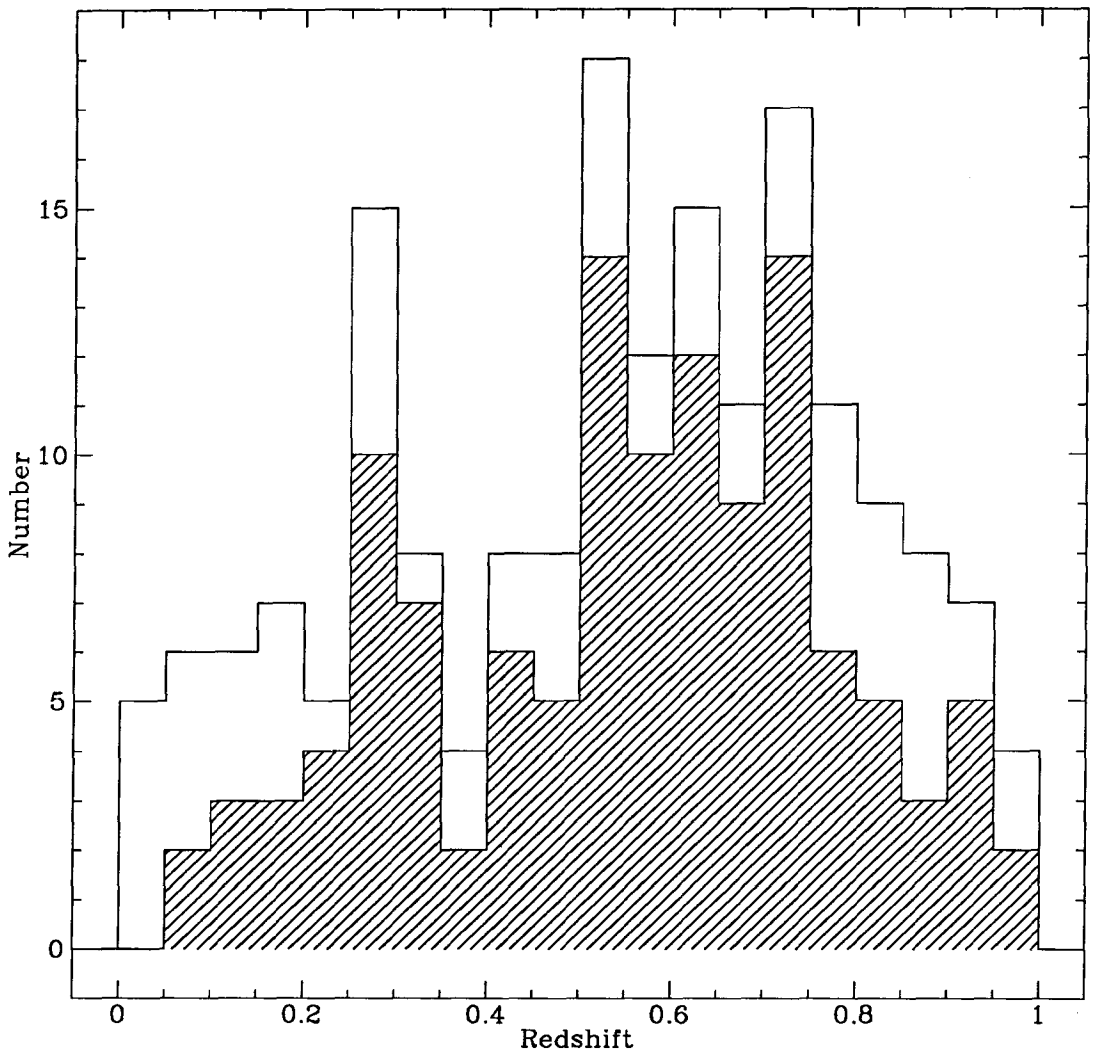

Figure 4.6: Distribution of the redshifts derived by template-fitting for all the objects in the field, shown by the solid histogram. The shaded histogram shows the distribution for objects classified as galaxies for both SEDs.

Table 4.6: Possible cluster members by redshift. The best-fit galaxy templates for these objects are at redshifts within 0.1 of the quasar redshift.

ID		Z	ΔZ	Gal.	Star	ΔRA	ΔDec	m_R	σ_{m_R}	S/N
147	S S	0.503	0.276	0.2	71.0	88.84	-24.10	22.28	0.40	2.5
151	G G	0.503	0.937	4.6	51.0	92.29	-84.71	20.99	0.12	5.3
11	S G	0.504	0.891	5.8	61.0	-141.53	-27.89	23.14	0.91	1.4
66	G G	0.505	0.018	3.8	67.0	-33.75	52.00	22.85	0.00	1.3
54	S G	0.506	0.844	5.8	48.0	-48.55	-49.24	22.81	0.57	1.3
23	G G	0.513	0.035	1.0	68.0	-121.56	-48.21	21.30	0.18	4.4
100	G G	0.514	0.000	0.3	71.5	5.85	48.21	23.13	0.00	1.3
52	G G	0.516	0.174	0.5	69.0	-57.16	37.19	22.84	0.75	1.2
170	G G	0.516	0.174	5.0	53.0	127.75	-90.56	23.05	0.00	1.3
21	G G	0.523	0.017	0.6	68.0	-125.69	-51.31	21.93	0.29	3.1
77	G G	0.524	0.158	0.8	70.0	-18.59	19.97	22.28	0.34	2.4
103	G G	0.527	0.228	3.5	64.5	10.33	-52.00	20.83	0.09	6.7
161	S S	0.529	0.540	1.3	67.0	116.39	78.17	15.68	0.04	27.5
115	G G	0.531	0.035	3.0	60.5	24.79	-17.56	22.94	0.00	1.6
173	G G	0.533	0.744	5.2	56.5	133.26	16.18	22.92	0.53	1.6
159	G G	0.535	0.212	5.2	65.0	103.65	4.13	22.85	0.52	1.3
65	G G	0.536	0.247	2.2	66.5	-35.12	-28.24	22.21	0.36	2.2
114	G G	0.540	0.018	3.6	57.0	24.79	86.78	21.44	0.21	3.3
44	G G	0.551	0.179	5.2	60.0	-76.79	-2.07	22.02	0.25	2.7
74	G G	0.558	0.054	5.5	61.5	-23.76	-42.70	21.78	0.24	3.1
87	G G	0.558	0.018	0.2	69.0	-7.23	14.12	21.10	0.17	4.4
120	G G	0.567	0.000	1.8	67.0	27.89	-71.28	22.35	0.34	2.5
179	G G	0.567	0.675	0.9	65.5	142.91	-101.24	23.01	0.92	1.0
83	G S	0.576	0.325	0.2	72.0	-12.74	-6.20	22.66	0.44	1.8
183	G G	0.577	0.127	3.0	65.5	146.00	-73.69	22.72	1.48	1.4
97	G G	0.578	0.834	4.2	54.0	2.75	68.18	23.24	1.06	1.2
96	G G	0.585	0.036	1.5	67.0	2.41	20.32	21.44	0.19	3.6
165	S G	0.585	0.036	0.0	75.5	123.28	-38.57	22.66	1.58	1.2

ID		Z	ΔZ	Gal.	Star	ΔRA	ΔDec	m_R	σ_{m_R}	S/N
64	G G	0.589	0.219	0.3	71.5	-39.60	-66.12	21.56	0.22	3.6
122	G G	0.591	0.293	6.0	60.0	32.71	25.14	23.20	0.00	0.8
135	G G	0.603	0.000	2.8	65.5	53.03	-44.42	22.34	0.36	2.5
58	G G	0.604	0.074	2.2	67.5	-45.11	-14.81	20.92	0.12	5.4
148	G S	0.605	0.111	0.1	71.0	88.84	12.05	23.64	0.00	0.8
63	G G	0.622	0.038	2.7	67.5	-40.63	14.12	22.84	0.51	1.5
42	G G	0.623	0.149	3.7	67.5	-77.48	95.04	22.90	0.85	1.6
172	G G	0.625	0.187	6.0	53.0	133.26	88.84	21.73	0.23	3.2
17	G S	0.632	0.057	2.5	66.0	-131.20	61.64	23.23	0.74	1.4
158	G G	0.632	0.131	0.0	72.0	103.31	-52.34	22.55	0.51	1.8
61	G G	0.634	0.632	6.0	31.5	-44.08	-107.09	23.23	2.23	1.2
48	G G	0.641	0.000	5.2	60.5	-62.67	97.80	21.36	0.16	3.9
154	G G	0.641	0.000	6.0	57.0	98.48	61.98	20.73	0.11	4.6
46	G G	0.650	0.095	1.8	69.0	-69.90	100.89	22.75	1.48	1.5
82	G G	0.650	0.019	3.8	64.0	-13.09	-71.62	23.02	0.61	1.5
104	S S	0.650	0.019	0.0	71.0	12.05	-8.26	22.63	0.55	1.9
150	G G	0.650	0.057	3.8	66.5	90.91	21.35	22.84	0.66	1.3
75	G G	0.660	0.038	1.5	71.0	-19.63	48.55	21.65	0.26	2.6
126	S S	0.660	0.000	1.8	71.0	39.94	-6.54	20.85	0.11	6.2
153	G G	0.667	0.306	5.2	64.5	94.01	-44.42	23.62	0.00	0.9
60	G G	0.669	0.057	2.7	67.0	-44.08	22.04	22.57	0.44	2.1
91	G G	0.672	0.646	1.9	67.5	-3.79	-19.63	22.84	0.70	1.7
136	G G	0.672	0.646	5.8	49.5	53.03	22.38	22.97	0.47	1.2
145	G G	0.672	0.646	3.0	52.5	82.99	22.38	23.28	0.00	1.1
12	S S	0.678	0.327	0.0	75.5	-141.53	26.51	23.34	0.00	1.1
133	G G	0.679	0.077	1.0	70.0	47.86	-61.98	22.52	0.48	1.5
111	G G	0.691	0.175	0.9	71.5	21.35	15.84	22.32	0.33	2.6
162	G G	0.698	0.000	0.3	70.5	116.39	35.12	22.24	0.65	2.4
128	G G	0.701	0.196	2.0	70.0	40.29	-11.71	21.64	0.25	3.3
131	G G	0.702	0.235	4.8	66.5	47.52	-11.71	22.92	0.65	1.4

cludes only the objects with median signal-to-noise ratio of 2.0 or more (99 objects) and of 3.0 or more (61 objects). Again, those objects classed twice as galaxies are shown by the shaded histograms.

Some apparent enhancement in the number of galaxies near redshift 0.6 is still seen in each of these distributions, again suggesting that some cluster galaxies are being detected. A more thorough statistical discussion of the significance of this apparent cluster cannot be made, due to the size of the redshift and magnitude errors and to the presence of the two biases described above. However, there is another enhancement in the number of galaxies with redshifts around 0.25 to 0.3, which is clearly seen in all three figures. The nearest redshift published by EGY was at z=0.3266, but they did not find evidence for a cluster at that redshift. Without obtaining spectra of these objects, we cannot be certain whether this enhancement represents a second cluster or just an artifact in the fitting process.

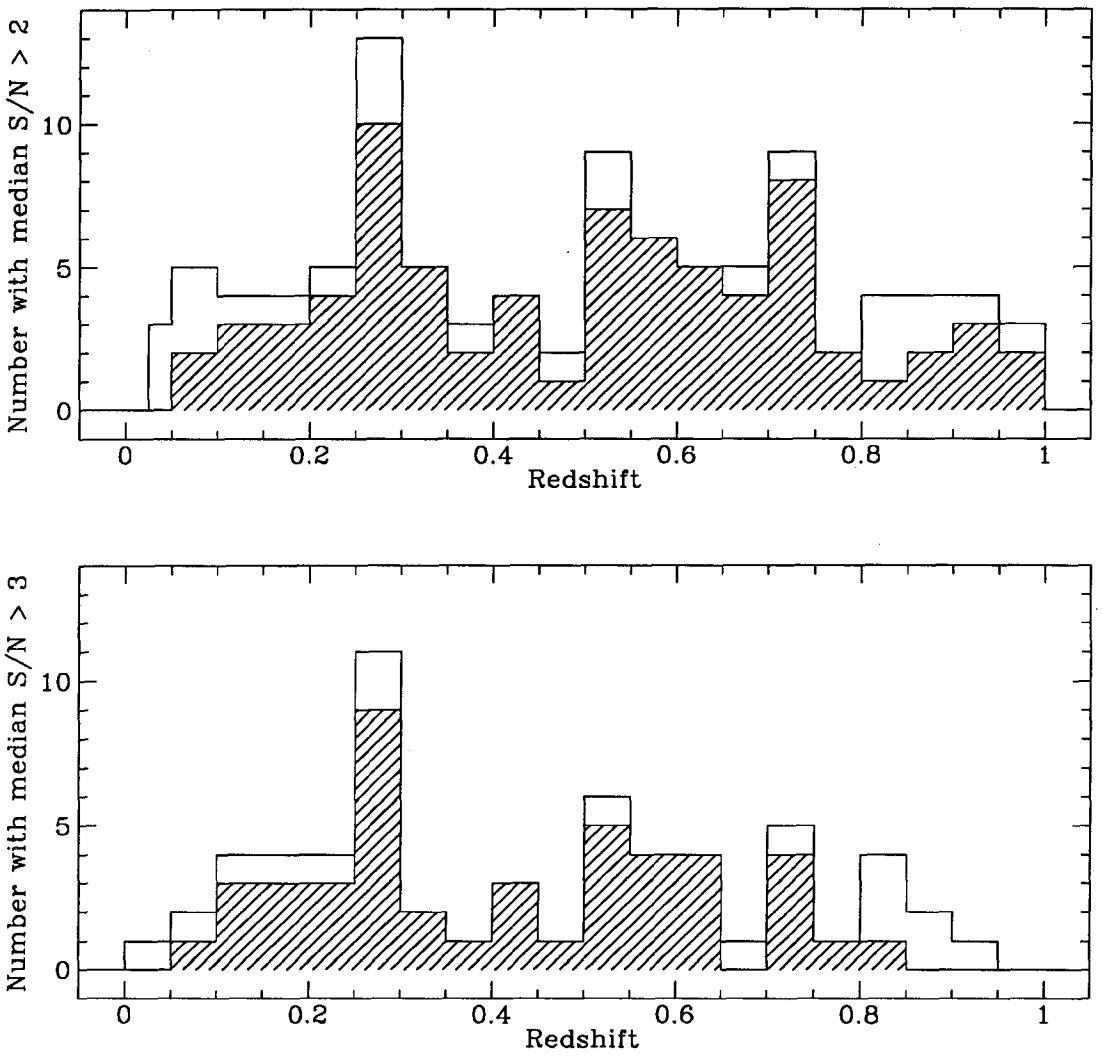

Figure 4.7: The distribution of the derived redshifts, for objects with median signal-to-noise ratio 2.0 or greater (upper plot) and 3.0 or greater (lower plot). The shaded histograms represent those objects classified as galaxies according to both SEDs.

Chapter 5

Broadband Magnitudes

The narrowband filters can be combined in such a way as to simulate the transmission curves of some standard broadband filters. Besides allowing presentation of the magnitudes of the objects in a recognizable form, this should make it possible, with the appropriate spectral coverage, to construct the filters used by Loh and Spillar or Koo, and compare results from SED-fitting with redshifts derived from optical multicolours.

Unfortunately, due to the spectral range and distribution of the filters used in this study, it was only possible to make a reasonable simulation of one filter, R. The R transmission curve modelled is from Bessell (1983). The transmission curves of twenty-one filters were each multiplied by an appropriate coefficient and combined to produce a model R filter transmission curve with the same area, in transmission-wavelength space, as the Bessell R. Both the real and the model R filters are shown in figure 5.1. The coefficients for the filters were chosen so that the difference between the areas is as small as possible regardless of the width of the spectral subregion considered.

The simulated filter will provide a good approximation of an R filter for flat-spectrum objects, and a less-good approximation for objects with steep spectra or other spectral features. Because of its comb-like shape, it would not be a satisfactory filter for studying objects with significant energy in emission lines, since the observed brightness would be

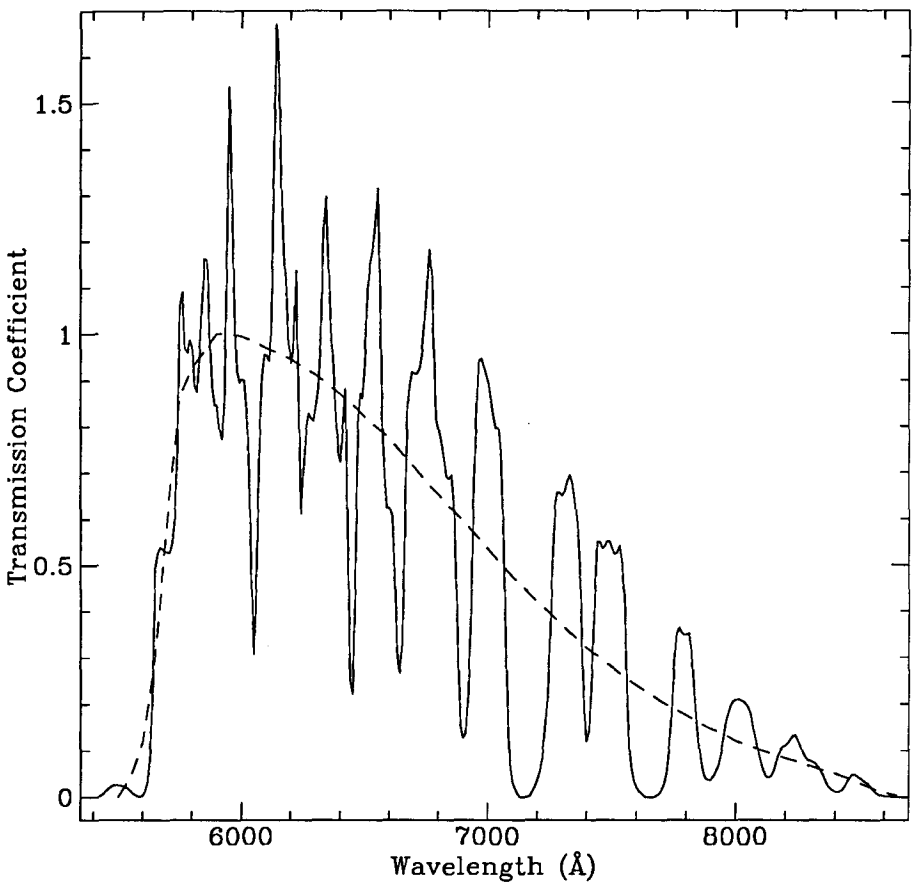

Figure 5.1: The true Bessell R filter is the dashed line, and the solid line represents a sum of narrowband filter transmission curves which have been multiplied by coefficients to simulate the broadband filter. The area below the two curves in wavelength-transmission space is the same.

a function of redshift (depending on whether or not the emission lines fall in the regions between peaks in the transmission curve).

To compute an "instrumental" r magnitude for an object, the total energy through the model R filter was computed as the sum of the coefficient (C_i) times the flux (f_i) in each filter:

$$m_{instr} = -2.5 \log_{10} \sum_{i=1}^{\#filters} C_i \times f_i.$$

Flux from the small aperture used to construct the SEDs was not used here, because a measure of all the light from the objects was sought. The possibility of using a single relatively large aperture was investigated, but the high sky contribution for objects of small angular size caused extra uncertainty in the fluxes for the faintest objects. For this reason the fluxes in the apertures selected by PPP's growth-curve algorithm were used. Although the growth-curve approach can underestimate the true flux value (as discussed earlier in section 3.1), the scatter in the R-magnitude calibration plot was smaller for growth-curve instrumental magnitudes than for those in a fixed large aperture.

Some objects are so faint in some filters that the subtraction of the background level leaves a negative signal. In these cases, PPP was not able to compute a magnitude, and the intensity for that filter was set to zero in the SED of the object. When such a point was encountered in the calculation of the instrumental magnitude, an interpolation was made from the fluxes in the two adjacent filters; that is, the intensity in each of the adjacent filters was divided by the equivalent width of the filter, then an interpolation (or extrapolation, in the case of a zero value in the first or last filters) was made, and finally the interpolated value was multiplied by the equivalent width of that filter to produce an estimated intensity.

The uncertainty in the instrumental magnitude is calculated by keeping a running sum of the total flux uncertainty over the contributions from the filters. This quantity is simply

the product of the flux in the filter, the fractional error of the flux ($\frac{\sigma_f}{f}$), and the model coefficient for the simulated R transmission curve. The resulting uncertainties range from 0.04 magnitudes for the QSO and a few of the brightest objects, to 2.5 magnitudes for the faintest galaxy, at magnitude $R = 23.37$. As expected, in general the estimated uncertainty in the r magnitudes of objects increases as the median signal-to-noise ratio decreases. This is illustrated by figure 5.2, which suggests that for objects with signal-to-noise ratio below about three or four, this technique does not supply useful R magnitudes.

R magnitudes for thirty-three objects in the field were obtained from Yee, Green, and Stockman (1986). These objects were used to establish the calibration between instrumental and true R magnitudes. The data for these objects is listed in table 4.5, and figure 5.3 shows the least-squares fit defining the calibration, which has the form $m_R = (0.992 \pm 0.013)\, m_{instr} - (13.267 \pm 0.253)$. The least-squares fit was weighted by the errors in the instrumental r magnitudes.

For interest, the distribution of the R magnitudes of the 184 objects in the sample is shown in the histogram in figure 5.4. This figure in no way represents a luminosity function for the field, because of the large uncertainties in the magnitudes of the faintest objects, and because no completeness correction has been made.

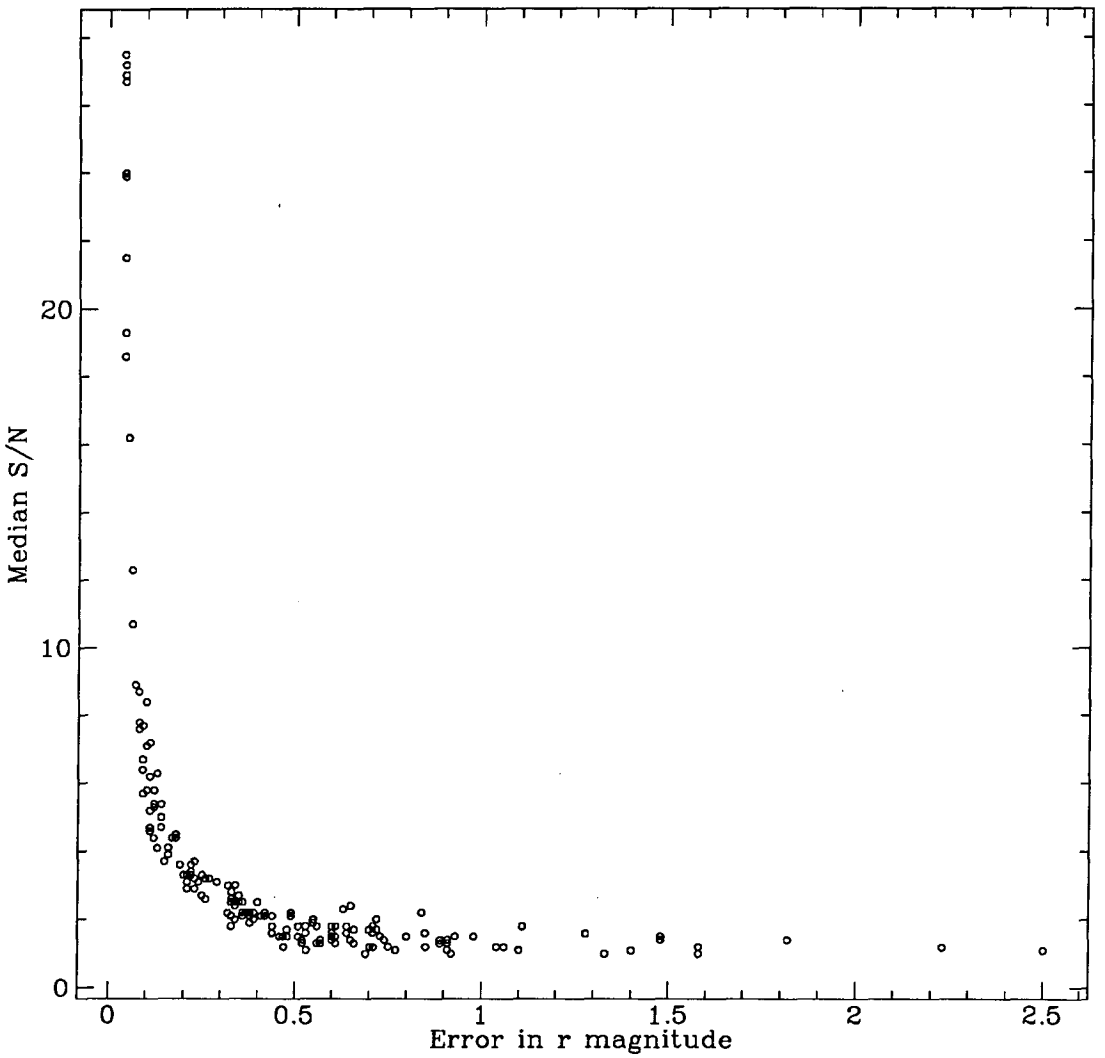

Figure 5.2: The estimated uncertainty in the simulated r magnitude shows a trend with median signal-to-noise ratio.

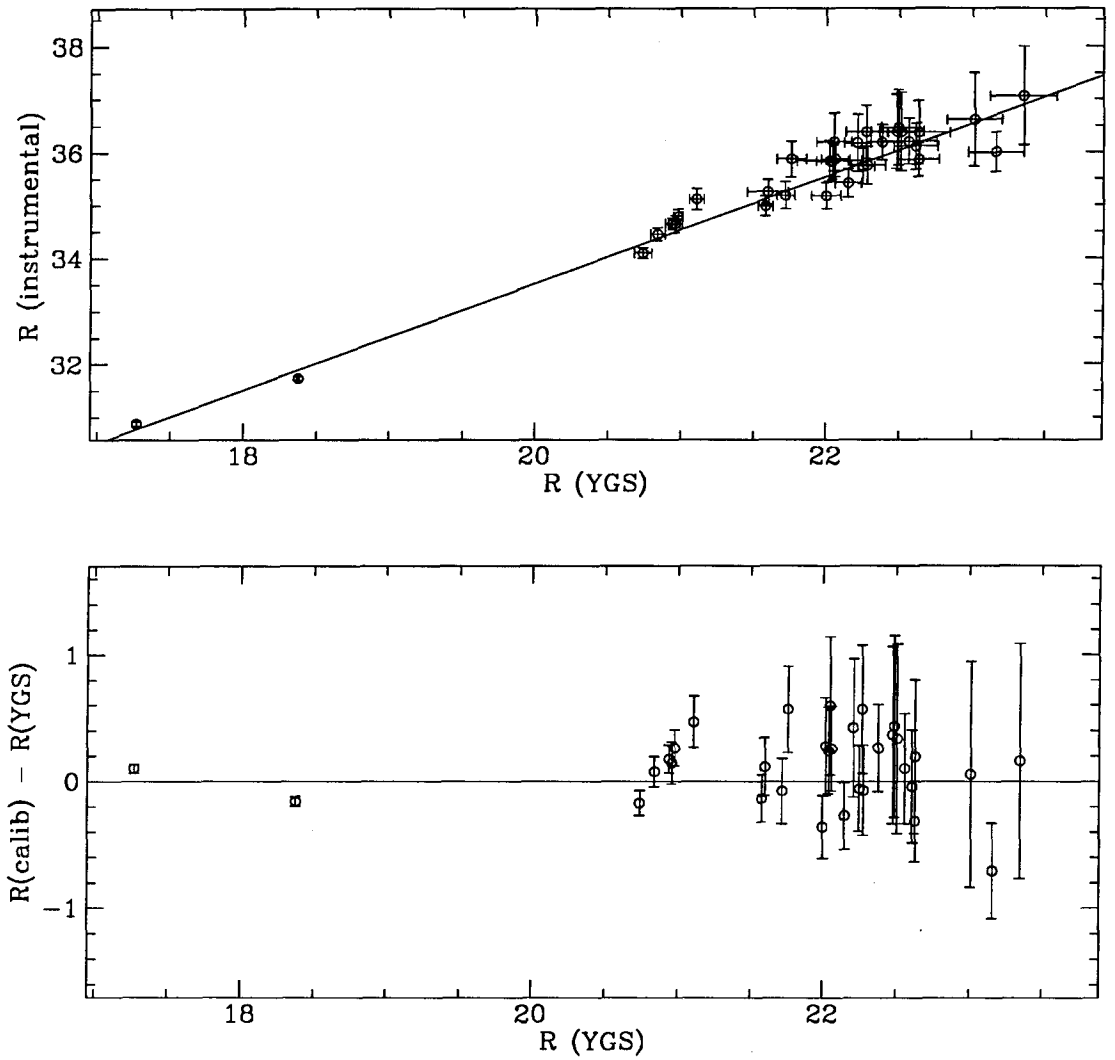

Figure 5.3: The instrumental r magnitudes were calibrated using R values from Yee, Green, and Stockman (1986). The first figure shows the calibration relation between the instrumental and the published magnitudes, and the second shows the deviation of the calibrated magnitudes from the fit.

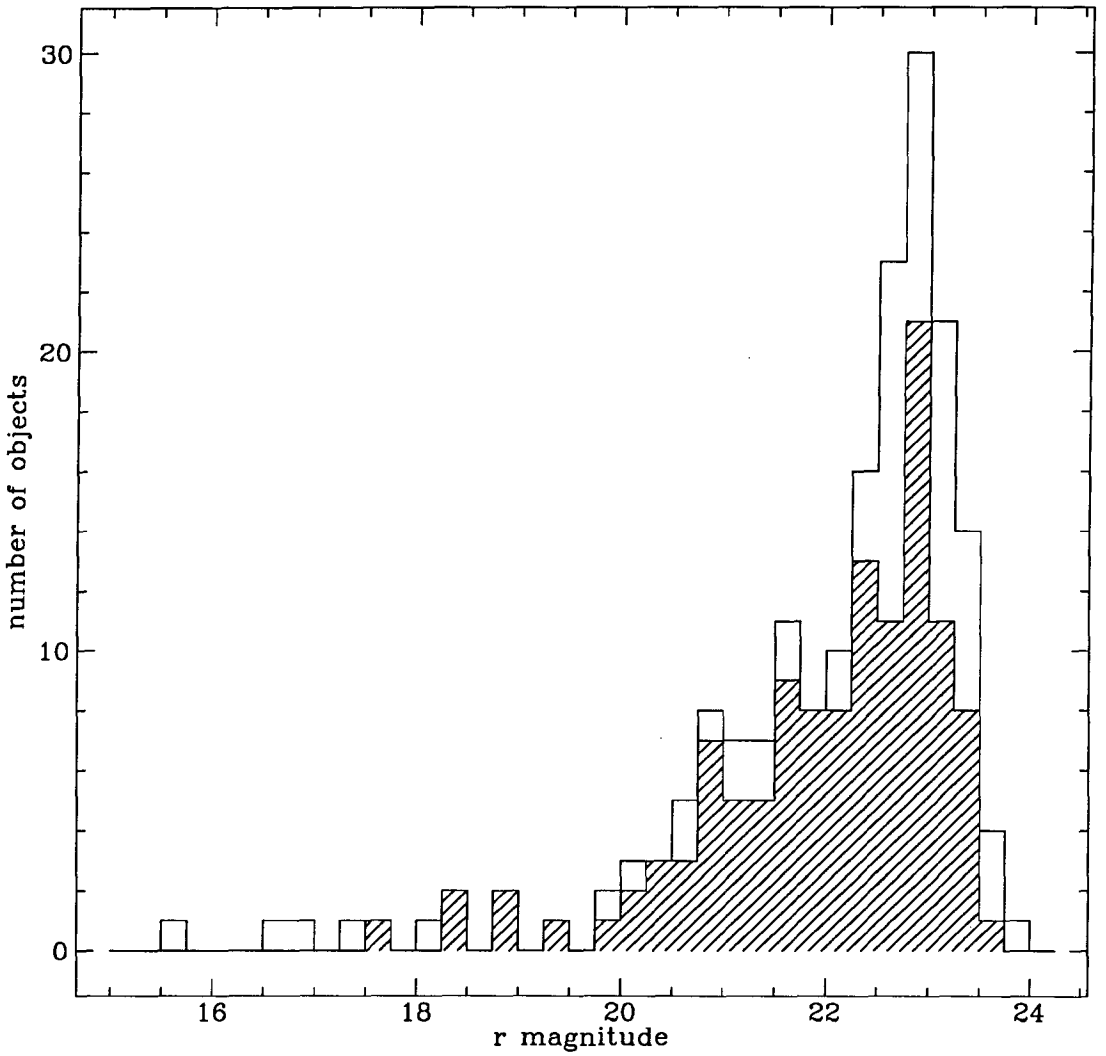

Figure 5.4: The distribution of the R magnitudes for the whole sample is shown by the solid-line histogram. The shaded histogram represents the magnitude distribution for those objects classified by the program as galaxies according to both SEDs.

Chapter 6

Accuracy of the Technique

It is crucial to understand the accuracy of redshifts and morphological classifications derived from multifilter spectrophotometry, if the technique is to be useful for other studies. A modelling analysis has helped evaluate the dependence of the results on the quality of the data and the type of object, but associating the modelling results with the quantities derived from real data in this study is difficult because there are so few objects in the sample for which the redshifts and physical identities are known. It has not been possible to investigate the accuracy of the morphological classification (*type* of galaxy or star) due to the lack of data of this sort for objects in the sample. Obtaining such comparison data spectroscopically would be quite demanding of telescope time because most of the field objects are very faint.

6.1 Results from Modelling

K. Callaghan, B. Gibson, and P. Hickson investigated the accuracy of the fitting technique using simulated observations in forty gaussian filters. The results of their study are currently in press (Hickson, Gibson, and Callaghan 1993). An interim report can be found in Callaghan, Gibson, and Hickson (1992), and a summary of the study to date in Callaghan (1992). Their goal was to investigate the effects of signal-to-noise ratio,

morphological type, and evolutionary state on the classifications and redshifts derived through template fitting.

Their approach was fairly straightforward. To construct an "observed" galaxy spectral energy distribution, they chose fiducial spectra from the atlas of Rocca-Volmerange and Guiderdoni (1988), defined an object-to-sky intensity ratio and a desired signal-to-noise level, then added to the model spectrum, random noise fluctuations of the appropriate size and a sky spectrum based on data from Turnrose (1974). The corresponding spectral energy distribution was made by multiplying this model spectrum by the forty filter transmission curves. Fitting of model templates was done in the same manner as for the real data presented in this thesis: χ^2 was calculated for each scaled template SED over a range of redshifts, and over a range of template ages as well, and the minimum χ^2 identified the best fit.

For each galaxy type investigated, ten different simulated observations were constructed at a given redshift and signal-to-noise level (from three to fifty), and the derived quantities from the fitting were averaged. The outcome of the study was summarized in the form of the error as a function of signal-to-noise ratio, for varying redshift at constant type and for varying type at constant redshift. For all types and redshifts, the error in both redshift and type decreases very clearly with increased signal-to-noise ratio. It is also observed that errors in type are larger for later-type galaxies than for E/S0s, and that errors in both type and redshift are reduced at higher redshifts. Callaghan (1992) concludes that redshifts derived from forty-filter spectrophotometry with signal-to-noise ratios of 3.0 or greater can be expected to have an error less than 0.12 for $z < 0.5$, and an error below 0.04 for objects at higher redshift.

The modelling study found that stars were rarely confused with galaxies, despite the similarities in their spectra. The best-fit stars to galaxy SEDs were types K and M for

ellipticals, G and K for early spirals, and A to G for late-type galaxies.

An important difference between the simulated observations used in the modelling and the real data in this study is the filter sets used. The set of forty gaussian filters, apart from having more points per SED, extends well into the blue, with the bluest filter at a central wavelength of 4000Å ($\log \nu = 14.875$). The model galaxy spectra in figure 4.2 demonstrate the importance of the blue end of the spectrum in distinguishing between shapes of the SEDs for different galaxy types. Redshifting causes the spectral differences to become more apparent, but because this study has only two widely separated filters blueward of 5500Å, galaxies must be at redshifts of 0.38 or more for the 4000Å break to be seen with any resolution. The filters used were chosen to make the break obvious at the cluster redshift (at z=0.602, the break is at 6400 Å), in expectation that this would allow galaxy velocities within the cluster to be accurately measured; however, it means that types and redshifts of low-redshift galaxies are very difficult to determine.

A secondary modelling study based on the filter set used to acquire the data in the 3C281 field was carried out, and the results are summarized in Callaghan, Gibson, and Hickson (1992). Using a signal-to-noise ratio of 5.0 for the simulated SEDs, they find that redshifts of early-type galaxies can be determined with an accuracy of 2%; for later-type galaxies, the redshift uncertainty is on order of 20%. The results also show, however, that "at low signal-to-noise ratios, it is possible to assign an anomalously high redshift to any local $z \approx 0.0$ galaxies". Morphological classification is observed to be accurate to within one type, and again they find no instance where a galaxy is misclassified as a star.

6.2 Accuracy of the Derived Quantities

It is of interest to examine the accuracy of the technique in distinguishing between star and galaxy SEDs, as well as in deriving the correct redshifts and types. The first

goal may be approached by comparing the classifications assigned by template-fitting with those derived by Yee according to the shape of the object for the objects in table 4.5.

If Yee's shape-dependent classifications are correct, then five out of thirty of the objects of "known" class (galaxy or star) in the 3C281 field data may have been erroneously classified by the fitting program. (Yee's list contains thirty-three objects, of which one is the QSO, and two others are galaxies that were too faint for the fitting program to classify.) Four of Yee's eight stars were classified as galaxies, but only one of twenty-two galaxies was best-fit by a star template.

The five objects have median signal-to-noise ratios of 1.7, 2.1, 2.2, 3.2, and 4.7 (the last is for the object identified as a star by SED-fitting). Objects with lower signal-to-noise ratios than these are assigned classifications that are the same as Yee's, so these are not "misclassified" because of their faintness. It is likely that some of the objects classified as stars by their shape and physical appearance are actually compact galaxies or bright galactic nuclei which appear pointlike because of their distance. The object classed as a galaxy by its shape but a star by its SED could be a galaxy of a type not represented by the models.

On the whole, classifications assigned by template-fitting to the SED correspond well with the classifications independently derived from the shape of each image.

It is also desirable to have a means of estimating the accuracy of the redshifts and morphological classifications produced by template-fitting. The only galaxies in the field for which redshifts are available are the twelve from EGY, listed in table 4.2.

The modelling results described in the previous section suggested a relationship between the signal-to-noise ratio of an object and the error in its assigned galaxy redshift. If such a relationship could be observed for this test sample, it could be extrapolated to describe the accuracy of the redshifts derived for objects at a given signal-to-noise ratio.

It should be kept in mind that EGY selected their galaxies based on magnitude ($r < 22.0$) and proximity to the quasar, and therefore the test sample may not represent the general population of objects seen in the field.

Using the twelve EGY galaxies, the redshift error is tested to see if it is related to properties of the object. One might expect, based on the modelling results, that the accuracy of the derived redshift would be related to the following quantities: the signal-to-noise ratio, since if the spectrum is better defined the model-fitting should be more accurate; the galaxy type, since early types have steeper spectra and their SEDs vary more in shape with redshift (e.g. see figure 4.3); and the redshift, since at higher redshifts the 4000Å break is shifted into the spectral region well sampled by the filter set. Figures 6.1 and 6.2 show the variation in redshift error with the three parameters listed above for the first and second sets of SEDs independently. The dashed lines in these figures are at redshift error of ± 0.1, a useful working limit for "acceptable" redshift errors.

The first set of SEDs yields seven redshifts within 0.1 of the true value, and an eighth that is close to being within the limit. Two of these objects, 44 and 128, have much worse assigned redshifts for their second SEDs. Both SEDs in each case appear equally noisy (figure 4.4), so it is unclear why one fit is good and the other bad. Object 44 has a fairly flat spectrum, which could contribute to confusion in the model-fitting, if the noise spikes are being treated as real spectral features in the fitting procedure.

Of the four objects with large redshift errors, two are classed as stars according to at least one SED. Object 92, classed once as a star, is assigned suspiciously high best-fit redshifts for the best galaxy fits to both SEDs. The data look no noisier for this object than for others which are assigned reasonable redshifts, but the spectrum is fairly flat, which means the noise is more likely to be fit by minor shape features in the models than it would be in a steeper spectrum. Object 95 also has very high assigned redshifts for the

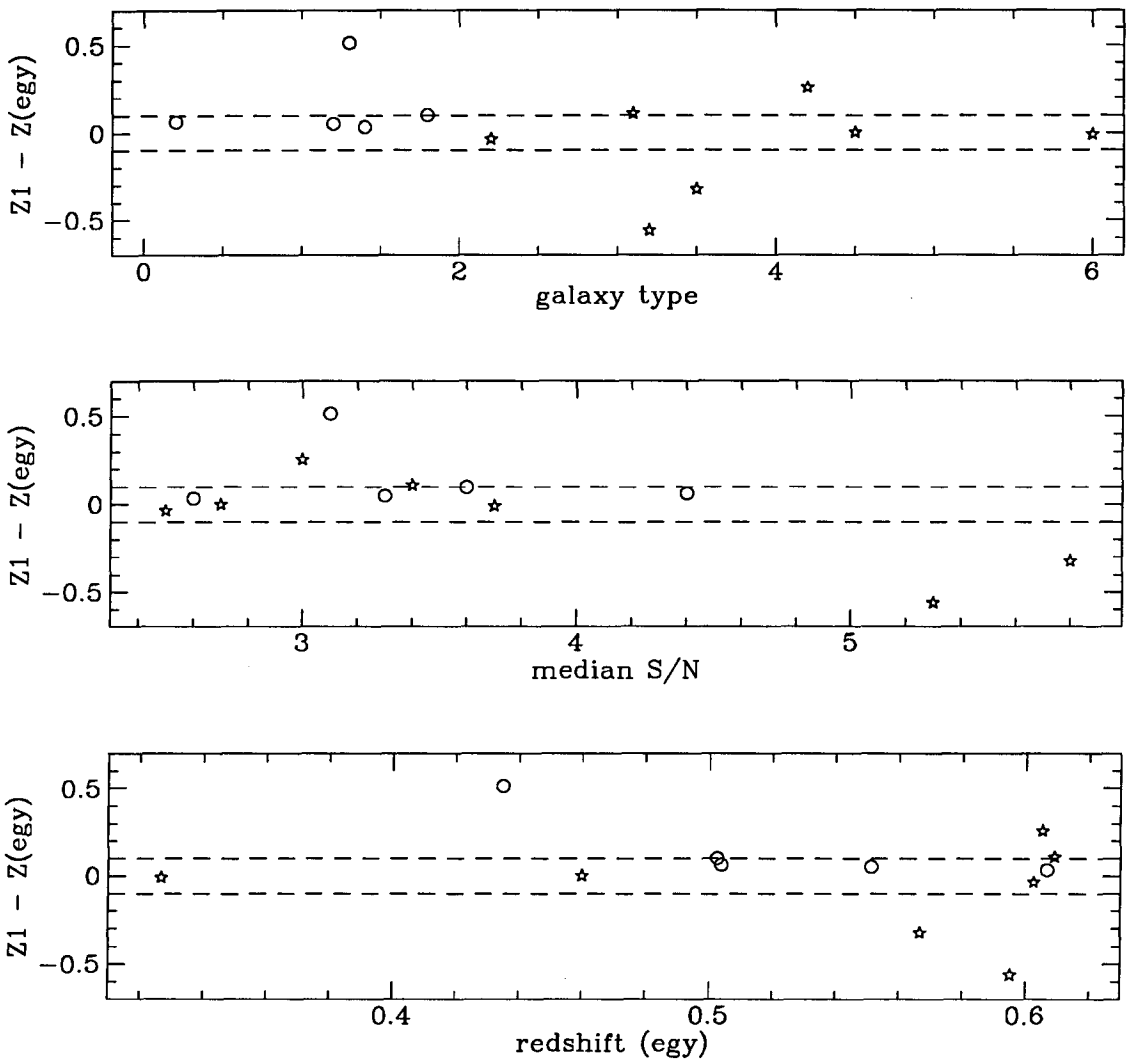

Figure 6.1: The y-axes of these plots are the accuracy of the derived redshifts for the first set of SEDs of the twelve galaxies from EGY. The accuracy is plotted as a function of galaxy type, median signal-to-noise ratio, and redshift. The hollow circles are the early-type galaxies, and galaxies of type 2.0 or later are represented by star-shaped points.

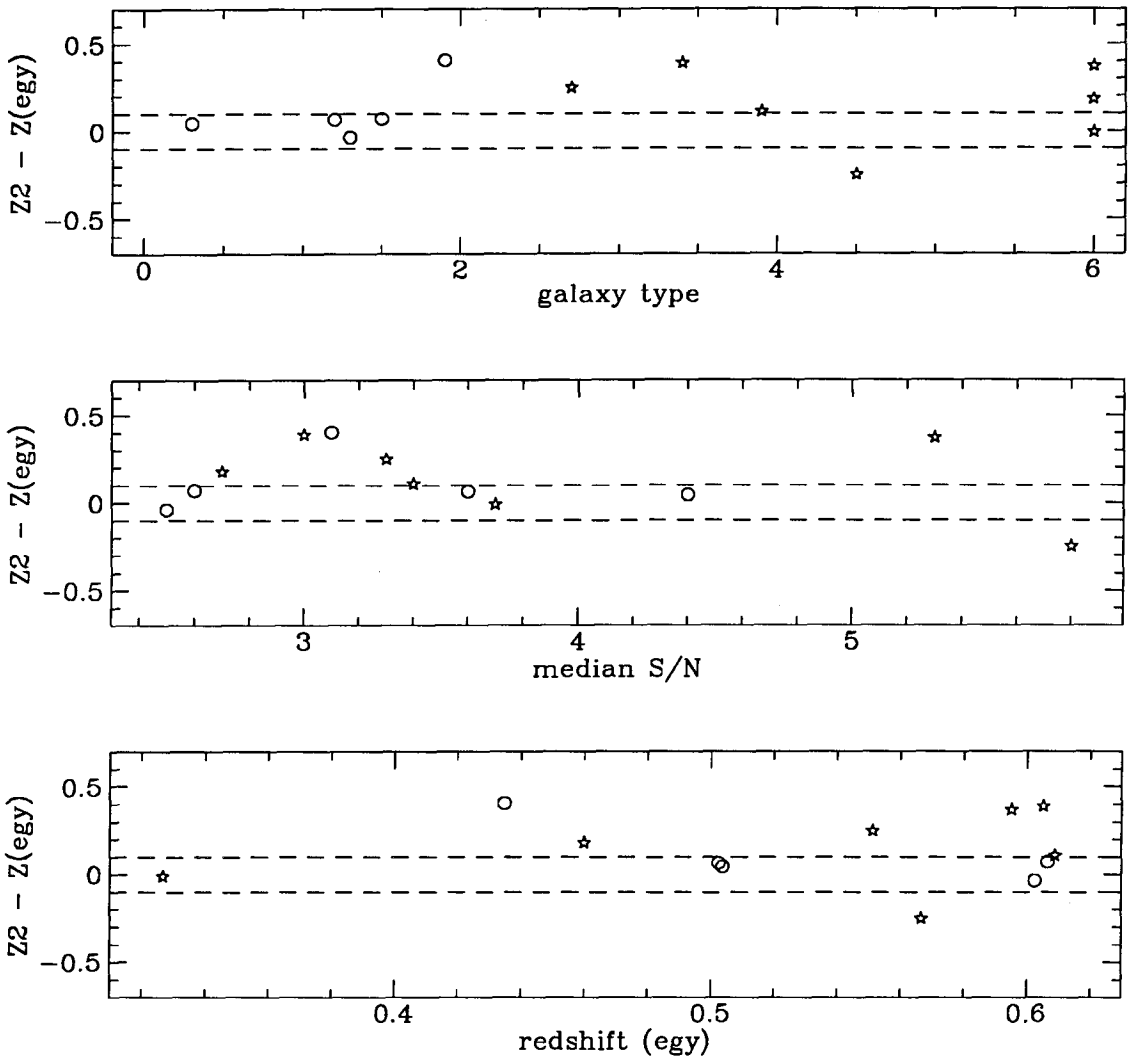

Figure 6.2: Redshift accuracies for the second set of SEDs of the EGY galaxies, as a function of galaxy type, median signal-to-noise ratio, and redshift. The hollow-circle points are the early-type galaxies, and the star-shaped points are the later types.

best-fit galaxy models, but both SEDs are classed as stars. The SEDs are steeper than those for 92, and again are not noisier than other SEDs with low redshift errors. Why the star spectra fit better is unknown, but it may be that the galaxy is of a type not represented in the set of models.

The other two objects with large redshift errors are 151 and 86. The SEDs of object 151 are so flat as to suggest that a definite redshift cannot be assigned, and noise in the models causes two different redshifts and galaxy types to be assigned. Object 86 appears to be well-fit by the two assigned galaxy models, which are at similar redshifts. It is possible that EGY's measured redshift for this object is in error, as H. Yee (pers.comm.) believes that 85-90% of the published redshifts in EGY were correct.

A survey of the two figures does not immediately reveal any of the anticipated correlations between redshift error and other properties. However, if object 95 is excluded (since both SEDs are best fit by a star model), then the early-type galaxies (up to type 1.9) all have redshift errors below the limit. This may have to do with the fact that the early-type galaxies are all at redshifts greater than 0.5, meaning that the 4000Å break is redshifted into a spectral region well sampled by the narrow filters. The galaxies assigned later types cover a wider range of redshifts, and no correlation is visible between accuracy and redshift; however, the 4000Å break is smaller for these objects.

There does not seem to be a significant relationship between median signal-to-noise ratio and redshift accuracy, as was suggested by the modelling study. However, there are no galaxies in the comparison sample with signal-to-noise ratio higher than six, and the sample itself is too small and limited to allow generalizations about the accuracy of the method to be made.

It is possible that the shape of a curve of χ^2 vs. redshift for a particular object could allow an estimate of the redshift accuracy to be made; and similarly, a curve of χ^2 vs.

model type could give an idea of the type accuracy. However, this would be most effective for well-defined SEDs. Most of the SEDs in this sample show signs of substantial noise in the photometry, and are not clear enough to yield a smooth curve of χ^2 with a single well-defined minimum; it is more likely that there exist a number of local χ^2 minima in redshift-type space.

With a larger sample of galaxies with known redshifts, and a wider range in signal-to-noise ratio, it might be possible to extrapolate the relationship between signal-to-noise ratio and expected error found in the modelling study, in order to estimate the redshift uncertainty for galaxies in the 3C281 field. Unfortunately, no such relationship can be defined using the sample of known-redshift objects available at present. It is only possible to agree with the well-known observation, discussed at length by Koo (1985) and upheld by the modelling study using the LMT filters, that it is much easier to obtain accurate redshifts based on the shapes of galaxy spectra for early-type galaxies than for later types.

Chapter 7

Discussion

Studies using simulated data suggest that accurate redshifts and object classifications can be derived from fitting templates to multi-narrowband filter spectral energy distributions. The simulations of Callaghan et al. (1992) using the same twenty-four filters that were used to produce the real data predict an error of 20% in the redshifts of late-type galaxies, with much better accuracy for early-type galaxies, based on trials with signal-to-noise ratio of 5.0. It is not appropriate to compare the results for the small sample of galaxies of known redshift with the modelling results, because only two galaxies observed have median signal-to-noise ratio above five, and neither yields a redshift within 0.1 of the published value. However, of the five galaxies assigned early types by template-fitting, four have acceptable redshifts, while the fifth is classed as a star and assigned an inaccurate redshift by its best-fit galaxy model. Three of the seven later-type galaxies have redshifts within 0.1 of the published value, and another is close. The overall accuracy of the derived redshifts is fairly good, especially in view of the reasons, suggested in section 6.2, why the four galaxies with incorrect redshifts may not be accurately identified.

The modelling results anticipated that no confusion would arise between galaxy and star templates, but one EGY galaxy is classified as a star according to both its independent SEDs, and another has a star template as the best fit to one SED. The misclassification

could occur because of noise in the SED, or because the object is of a type not represented in the set of model spectra, such as an emission-line object.

Errors in the photometry which contribute to misclassification can arise within the derived uncertainty term, or from possible extinction in the observations made on one night. A further source of error may arise in the calibration, particularly if a spectral line in the standard star's spectrum lies within one of the filters. A search for systematic errors was made by comparing EGY galaxy SEDs with the best-fit models yielding correct redshifts. Total intensities for all the objects were scaled accordingly, and best-fit types and redshifts derived. However, this procedure did not improve the average goodness-of-fit to models, and produced slightly poorer redshifts for the EGY sample, as compared to results from spectral energy distributions where only the points from the 6200Å filter were adjusted. The latter set was used for the analysis described in the previous chapters.

It is stressed that high-quality photometry will yield the best object identifications. The results presented here are the second set to be derived from these data. The first version included several extra sources of error in the photometry, and the accuracy was visibly poorer than that seen in these results.

Although the comparison sample of known-redshift galaxies did not cover a wide range of redshifts, it is expected that better sampling at the blue end of the SED would be of great value in helping discriminate between low-redshift objects and high-redshift later-type galaxies.

If good-quality, non-comatic images are used, it might be possible to assign an object a galaxy or star class based on its shape, before trying to fit models to its SED. This would eliminate some of the confusion due to the similarity of model galaxy and star spectra, although comparisons with shape-derived classifications supplied by Yee suggest that there are few instances where the fitting program cannot distinguish stars from

galaxies at reasonable signal-to-noise ratio (section 4.6). Since galaxy images, and images of other interesting non-stellar objects, can be circular as well as extended, all compact objects would have to be fitted with both star and galaxy models, but the extended objects would not have to be fitted with star models. It was not possible to pre-classify objects in this way with the data set used, because the obvious coma near the edges of the images suggests some degree of image distortion for many objects in the field.

Standard broadband filter photometry can be simulated by combining the fluxes from the narrowband filters multiplied by appropriate coefficients. The accuracy of the simulated photometry is not yet known, although there is quite a large scatter as shown in the calibration diagram, figure 5.3. A second data set is available, for the field of the quasar PKS 0812+020, and this will serve to investigate the accuracy of the "multifilter broadband colours" in the near future. With suitable spectral coverage, it should prove possible to simulate other broadband filters, and perhaps to compare the redshifts derived from template-fitting with redshifts from optical multicolours, as done by Koo (1985) and others. The UBC LMT data will be extremely versatile in this respect, since the forty filters to be used overlap well and cover the same spectral range as the V, R, and I filters, and most of the B filter as well. The transmission curves of the LMT filter set and the broadband filters are shown in figure 7.1.

The second data set will be useful not only in testing the accuracy of the broadband photometry, but also for further analysis of the accuracy of the method. EGY have published redshifts for thirteen objects in the field of PKS 0812+020, which lies at a redshift of 0.403. If all these objects are detected in the CCD photometry of the field image, they will double the size of the sample of galaxies with known redshifts, and may help define a relationship between signal-to-noise ratio and redshift accuracy, which could not be done using the comparison sample from the 3C281 field alone.

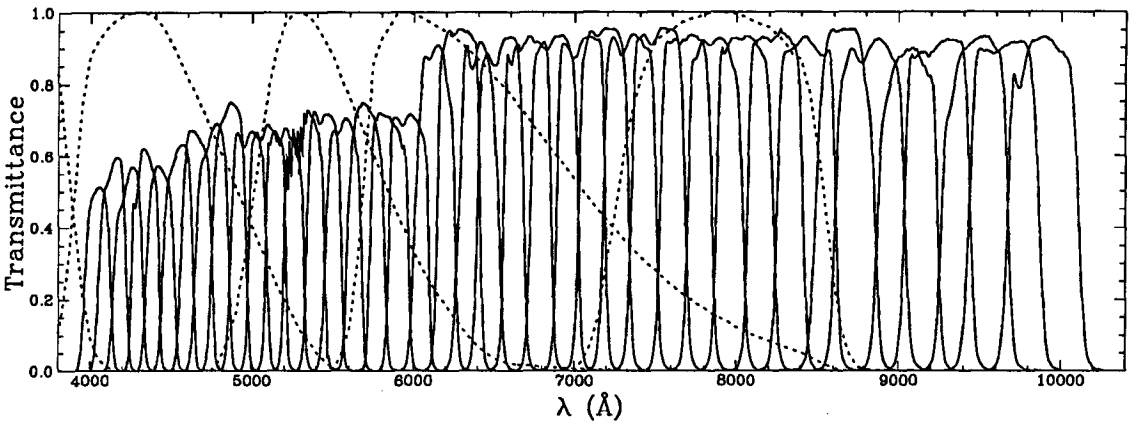

Figure 7.1: The transmission curves of the UBC Liquid Mirror Telescope filter set. Standard broadband filters are shown as dotted lines: the filter set covers (from lowest to highest wavelength) most of the B filter, and all of the V, R, and I filters. (This figure is provided courtesy of B.K. Gibson.)

Chapter 8

Conclusion

The technique of deriving galaxy redshifts by fitting models based on template spectra to the spectral energy distributions produced by multi-narrowband-filter photometry appears to be fairly successful, although the results presented here are not entirely conclusive. The levels of accuracy predicted by the modelling study cannot be confirmed, but the derived redshift values for objects of known redshift give reason for optimism. An enhancement in the number of galaxies with derived redshifts near that of the QSO, where a cluster is expected, further suggests that the derived redshifts are fairly close to the true values.

Though results from simulated spectral energy distributions show a clear relationship between the signal-to-noise ratio of the observations and accuracy of the derived redshift, the real data for objects in the field of the quasar 3C281 showed no such relationship. However, there were only twelve galaxies in the field with known redshifts, and these all had median signal-to-noise ratios below six, so whether or not a signal-to-noise ratio—redshift-accuracy relation exists for the data is still undetermined.

What is clear from the results for the galaxies of known redshift is that the redshifts derived from template-fitting for galaxies classified as E/S0 are more likely to be accurate than are the redshifts for objects fit as later-type galaxies. This is to be expected, as

the 4000Å break is much more pronounced in the spectra of early-type galaxies, and can therefore be seen more easily when it is redshifted into the spectral domain of the filter set. It is observed that four of five early-type galaxies of known redshift, with signal-to-noise ratio greater than 2.0, have derived redshifts within 0.1 of their spectroscopic redshift (and the fifth is best-fit by a star model), while three of seven later-type galaxies (and nearly one more) have redshifts errors of this magnitude.

Thirty-two objects in the observed field, which were independently classified by H. Yee as galaxies or stars depending on image shape, were used to test the accuracy of type classification. Tests with simulated data, using both the forty-point LMT filter set and the twenty-four filters used for these data, indicated no confusion between galaxies and stars even at low signal-to-noise ratios. In practice, the template-fitting method yielded the same classes as the shape criterion for two out of six of Yee's stars and twenty of twenty-one galaxies. The remaining five objects (two stars and three galaxies according to Yee) were too faint to be consistently fit: the best fit to one SED was a star and to the other, a galaxy. It is entirely possible that some of the objects with the shapes of stars could actually be compact galaxies or nuclei, which would explain the galaxy classifications assigned to the four objects of stellar appearance.

The same list of objects, with the QSO added, was used to calibrate the instrumental r magnitudes produced by combining narrowband filters. The estimated uncertainty in the R thus produced ranged from 0.04 magnitudes for the brightest objects to 2.5 magnitudes for a galaxy of magnitude 23.4. With a suitably high level of signal-to-noise ratio data, it should be possible to do broadband photometry with multi-narrowband-filter data.

The results of this study, despite the low number of comparison objects of known redshift, suggest that useful redshifts and type classifications can be obtained from the method of multifilter spectrophotometry even at signal-to-noise of three or below. The

most immediate need is for a larger sample of objects with known redshifts, so that a more complete analysis may be made of the accuracy of quantities derived by the template-fitting procedure. Improved spectral resolution, higher signal-to-noise data, and better sampling in the blue end of the spectrum as in the LMT filter set, can only improve upon the results described here.

Bibliography

Baum, W.A. 1962, in *Problems of Extragalactic Research*, IAU Symposium 15, ed. G.C. McVittie (New York: MacMillan) p. 390

Bessell, M. 1983, PASP 95, 480

Bevington, P.R. 1969, *Data Reduction and Error Analysis for the Physical Sciences*, (New York: McGraw-Hill)

Bruzual, G. 1983, ApJ 273, 105

Burstein, D., and Heiles, C. 1978, ApJ 225, 40

Butcher, H., and Oemler, A. 1978, ApJ 219, 18

Callaghan, K. 1992, *Multi-Filter Spectrophotometry Simulations*, unpublished report

Callaghan, K., Gibson, B.K., and Hickson, P. 1992, in *The Evolution of Galaxies and Their Environment*, eds D. Hollenbach, H. Thronson, and J.M. Shull, NASA Conference Publication 3190, page 357

Canada-France-Hawaii Telescope Corporation 1990, *Users' Manual*

Cardelli, J.A., Clayton, G.C., and Mathis, J.S. 1989, ApJ 345, 245

Couch, W.J., Ellis, R.S., Godwin, J., and Carter, D. 1983, MNRAS 205, 1287

Couch, W.J., and Newall, E.B. 1980, PASP 92, 746

de Vaucouleurs, G., de Vaucouleurs, A., and Corwin, H.G. Jr. 1976, *Second Reference Catalogue of Bright Galaxies* (Austin, Texas: University of Texas Press)

Ellingson, E., Green, R.F., and Yee, H.K.C. 1991, ApJ 378, 476

Ellis, R.S., Couch, W.J., MacLaren, I., and Koo, D.C. 1985, MNRAS 217, 239

Gibson, B.K, and Hickson, P. 1991, in *The Space Distribution of Quasars*, ed. D. Crampton (ASP: San Francisco)

Guiderdoni, B., and Rocca-Volmerange, B. 1987, A&A 186, 1

Gunn, J.E., and Stryker, L.L. 1983, ApJS 52, 121

Hickson, P., Gibson, B.K., and Callaghan, K. 1993, MNRAS, submitted

Hickson, P., Gibson, B.K., and Hogg, D.W. 1993, PASP, in press

Hickson, P., Richardson, E.H., and Grundmann, W.A. 1992

Koo, D.C. 1981, ApJ 251, L75

Koo, D.C. 1985, AJ 90, 418

Kron, R. 1980, ApJS 43, 305

Lang, K. R. 1986, *Astrophysical Formulae* (New York: Springer-Verlag)

Loh, E.D., and Spillar, E.J. 1986, ApJ 303, 154

MacLaren, I., Ellis, R.S., and Couch, W.J. 1988, MNRAS 230, 249

Mathieu, R.D., and Spinrad, H. 1981, ApJ 251, 485

Mihalas, D. and Binney, J. 1981, *Galactic Astronomy – Structure and Kinematics*, (New York: W.H. Freeman & Co.)

Oke, J.B. 1966, ApJ 145, 668

Oke, J.B. 1969, P.A.S.P. 81, 11

Oke, J.B., and Gunn, J.E. 1983, ApJ 266, 713

Oke, J.B., Neugebauer, G., and Becklin, E.E. 1970, ApJ 159, 341-355

Oke, J.B., and Schild, R.E. 1970, ApJ 161, 1015

Ratnatunga, K., and Bahcall, J. 1985, ApJS 59, 63

Rocca-Volmerange, B., and Guiderdoni, B. 1988, A.&A.Supp. 75, 93

Sandage, A. 1988, ARAA 26, 561

Sandage, A., and Tammann, G.A. 1987, *A Revised Shapley-Ames Catalog of Bright Galaxies*, Carnegie Institute of Washington Publication 635

Spinrad, H. 1980, in *Objects of High Redshift*, IAU Symposium No. 92, ed. G. Abell and P.J.E. Peebles, (Dordrecht: Reidel), p.39

Turnrose, B.E. 1974, PASP 86, 545

Valdes, F. 1982, *Faint Object Classification and Analysis System*, Kitt Peak National Observatory, Tucson

Wampler, E.J. 1966, ApJ 144, 921

Wampler, E.J. 1967, ApJ 147, 1

Yee, H.K.C. 1991, P.A.S.P. 103, 396

Yee, H.K.C., Green, R.F., and Stockman, H.S. 1986, ApJS 62, 681